Journal of Rock Mechanics and Geotechnical Engineering 18 (2026) 3365–3393

Contents lists available at ScienceDirect

Journal of Rock Mechanics and Geotechnical Engineering

journal homepage: www.jrmge.cn

Full Length Article

A novel hybrid surrogate model for the stability and post-failure analysis of spatially variable slopes using a smoothed sequential limit analysis

H. Xu [a], H.C. Nguyen [b,*], M. Nazem [c], X. He [d], X. Chen [e], R. Sousa [e], J. Kowalski [f]

[a] Faculty of Civil Engineering and Architecture, Xi'an University of Technology, Xi'an, China
[b] Faculty of Civil Engineering, HUTECH University, Ho Chi Minh City, 70000, Viet Nam
[c] Department of Civil and Infrastructure Engineering, School of Engineering, RMIT University, Melbourne, Australia
[d] School of Civil and Environmental Engineering, University of Technology, Sydney, NSW, 2007, Australia
[e] New York University Abu Dhabi, Abu Dhabi, United Arab Emirates
[f] Methods for Model-based Development in Computational Engineering, RWTH Aachen University, Aachen, Germany

ARTICLE INFO

Article history:
Received 31 December 2024
Received in revised form
19 July 2025
Accepted 14 September 2025
Available online 22 January 2026

Keywords:
Mixed formulation of limit analysis (MFLA)
Node-based smoothed finite element method (NS-FEM)
Multi-downsampling hybrid Linformer-CNN
Slope stability
Deep learning (DL) surrogate models

ABSTRACT

This study presents a novel framework for evaluating slope stability in spatially variable soils by integrating a newly developed sequential limit analysis based on the Hellinger-Reissner functional, utilizing the node-based smoothed finite element method (NS-FEM), with a newly proposed deep learning (DL) approach termed multi-downsampling hybrid Linformer-convolutional neural networks (CNNs). The NS-FEM-based mixed formulation of limit analysis (MFLA) enhances computational accuracy and convergence by smoothing strain fields and mitigating numerical discontinuities commonly encountered in standard finite element methods (FEMs). This method generates reliable datasets for stochastic simulations of slope stability under both static and seismic loading conditions. To address the computational expense of specific simulations, we propose the multi-downsampling hybrid Linformer-CNN model, a sophisticated DL architecture that employs dual parallel pathways with distinct downsampling strategies – AveragePpooling1D for medium-scale feature extraction and MaxPooling1D for coarse-scale feature extraction. Each pathway integrates one-dimensional (1D) CNNs for local feature extraction and Linformer-based self-attention mechanisms to efficiently capture global dependencies. The parallel downsampling strategies balance computational efficiency with feature granularity, enabling the model to leverage both local and global data characteristics effectively. The extracted multi-scale features are concatenated and further processed through fully connected networks (FCNs) to accurately predict the factor of safety (FoS) of slopes. Comparative analyses demonstrate that the hybrid Linformer-CNN model outperforms traditional FCN and CNN architectures, achieving robust and precise predictions with a mean absolute percentage error (MAPE) below 10 %. Additionally, the proposed framework significantly reduces computational time, highlighting the potential of integrating NS-FEM-based MFLA with advanced DL architectures for rapid and reliable slope stability assessment in geotechnical engineering.

1. Introduction

Landslides are among the most serious natural disasters worldwide, characterized by rapid onset, long runout distances, and massive movements of materials (Xing et al., 2014; Tang et al., 2015; Dang et al., 2016). Large numbers of fatalities can be attributed to very rapid and extremely rapid landslides, which move faster than a person can run (Turner, 2018). Landslides have complex and changeable inducing factors, such as rainfall infiltration, earthquakes, and human activities (Gariano and Guzzetti, 2016). Landslides are probably the most destructive secondary geotechnical hazard associated with earthquakes and ground vibrations (Valagussa et al., 2019). Accurate prediction of seismic

* Corresponding author.
E-mail address: nc.hoang@hutech.edu.vn (H.C. Nguyen).

Peer review under responsibility of Institute of Rock and Soil Mechanics, Chinese Academy of Sciences.

https://doi.org/10.1016/j.jrmge.2025.09.033

landslides is essential to ensure safety and mitigate risks. Slope stability analysis (e.g. assessing FoS and forecasting potential failures) emerges as a fast and effective method that can provide a comprehensive understanding of the likelihood of landslide occurrence and help to implement preventative measures.

Deterministic analyses are typically employed for evaluating slope stability in geotechnical engineering, wherein only mean values of soil properties are considered in simulations. However, soils exhibit significant spatial variability due to complex sediment deposition processes, such as weathering, transportation, and erosion (Phoon and Kulhawy, 1999). Deterministic calculations that disregard this spatial variability can significantly underestimate the risk of slope failure (Griffiths and Lane, 1999; Griffiths and Fenton, 2004; Chen et al., 2021; Liu et al., 2023). To solve this problem, random field theory is introduced to account for the spatial variability of soils. The random finite element method (RFEM) has been widely developed for estimating the probability distribution of slope stability (Liu and Wang, 2021; Wang et al., 2021a, b; Hsiao et al., 2022; Xu et al., 2022) and landslide runout distance (Chen et al., 2021, 2025; Liu et al., 2023; Ren et al., 2023). RFEM combines finite element analysis with random field theory to transform the stability analysis of spatially variable slopes into a probabilistic analysis problem with uncertainty.

Traditional RFEM performs brute-force analysis based on Monte Carlo sampling (Kroese et al., 2014; Chen et al., 2022; Aminpour et al., 2023a, b; Xu et al., 2023). However, the brute-force Monte Carlo approach, where the FoS of each Monte Carlo sample is evaluated using the numerical model, is both time-consuming and computationally intensive, especially when evaluating a small failure probability of structures (Chen and Li, 2017). Response surface method (RSM) was initially proposed to reduce the sample size required for reliability analysis (Kaymaz and McMahon, 2005; Allaix and Carbone, 2011). This method approximates the limit state function with a polynomial expression using the function value at a specific point. By replacing the exact limit state function with this analytical approximation in Monte Carlo simulations, RSM significantly reduces the computational efforts required to assess the reliability of structural systems. However, RSM requires a prior specification of a suitable fitting function (usually a polynomial function) (Desai et al., 2008). Owing to the inherent complexity of many real-world problems, polynomial estimates may struggle to adequately represent the objective function, resulting in reduced accuracy (Abbasi and Mahlooji, 2012).

In recent years, the use of machine learning (ML) techniques to develop surrogate models has gained tremendous popularity (He et al., 2020; Phoon and Zhang, 2023). This updated approach involves generating random field samples, conducting a relatively small number of random finite element simulations, training ML models, and subsequently using the well-trained models to predict slope stability and perform statistical analysis (such as failure probability). The integration of ML into geotechnical engineering has unlocked new possibilities for handling complex stochastic problems with reduced computational resources. Surrogate models, including support vector machines (SVMs) (Kang et al., 2016) and artificial neural networks (ANNs) (He et al., 2020), have demonstrated exceptional potential for lower computational costs while maintaining prediction accuracy. By leveraging high-fidelity models built from a limited set of finite element simulations, ML techniques enable researchers to efficiently perform probabilistic analyses and estimate slope stability.

Deep neural networks are the most successful deep learning (DL) method. The term 'deep' can refer to a structure of more than one hidden layer in ANNs. A convolutional neural network (CNN) is a commonly used DL model, which is widely used in image and pattern recognition (Szegedy et al., 2015; He et al., 2016) in the computer field, and has been extended to other fields, such as foundation bearing capacity problems (He et al., 2024) and slope stability problems (Liu et al., 2014; He et al., 2020; Wang and Goh, 2021; Zhang and Zhang, 2021; Wang, 2022; Aminpour et al., 2023a, b; Huang et al., 2023; Xu et al., 2023) in geotechnical engineering. Hidden CNN layers usually include several stacks of convolutional and pooling layers, which are then connected to a fully connected layer to build the regression model. Convolutional layers use kernels to extract spatial features from input data. In contrast, pooling layers can reduce the resolution of convolutional outputs while preserving key information. It has been proven that trained CNNs are an alternative approach to computationally demanding physics-based simulation models for Monte Carlo simulations, which can learn the high-level uncertainty of both input and output data. Also, there are some variants of CNNs, such as locally connected networks (Xu et al., 2023; He et al., 2024). Classic deep neural network (DNN) structures include recurrent neural networks (RNNs), transformers, etc. RNNs can be used to process language models (Mikolov et al., 2010) and speech recognition (Graves et al., 2013). Long short-term memory (LSTM) is a popular variant of RNNs. The recently very popular ChatGPT from OpenAI is based on the transformer architecture (Brown, 2020). DNNs usually have many layers and millions of parameters, which can help models fit the training data closely. However, overcomplicated model structures can lead to overfitting problems (the generalization of the trained model is poor). This problem is usually avoided using regularization or trimming connectivity (dropout, etc.).

Local connected neural networks (LCNs) are a type of neural network architecture that allows for localized connectivity patterns in layers. They are similar to CNNs but without the weight-sharing characteristic of CNNs. In LCNs, each neuron in a given layer is connected only to a small, localized region of the previous layer. This unique feature allows the network to capture local patterns without requiring a full connection to all neurons. Unlike CNNs, where the same kernel weights are applied across the entire input, LCNs have distinct weights for each local connection, providing them with a high degree of flexibility in learning features specific to different input regions. This adaptability makes LCNs particularly useful in scenarios where distinct local features must be captured, but global features are either irrelevant or can be handled differently. They can be applied in tasks such as image recognition and processing, especially when objects vary in size and position within the input space. The computational cost can dramatically increase due to the more significant number of parameters compared to convolutional layers, as each local region has its own unique set of weights. While they differ in weight sharing, LCNs share some benefits with CNNs, such as translational invariance to local features, which can aid in tasks requiring pattern recognition. It is reasonable to conclude that LCNs provide an alternative approach to capturing localized features without enforcing the constraints of weight sharing found in typical CNN architectures.

A central component of the transformer model is the self-attention mechanism, which simultaneously models dependencies between every element (token) in a sequence and all other elements, thereby extracting global contextual information in a single computation (Vaswani et al., 2017). Practically, self-attention assigns three vectors to each element: query ($\boldsymbol{Q}$), key ($\boldsymbol{K}$), and value ($\boldsymbol{V}$), and uses the dot product between $\boldsymbol{Q}$ and $\boldsymbol{K}$ to determine which positions in each element of the sequence attend to. By employing multiple attention heads (multi-head attention) in parallel, the model can focus on diverse features from different subspaces, enhancing the richness and precision of the extracted

information (Vaswani et al., 2017; Devlin, 2019). Compared to traditional recurrent or convolutional structures, self-attention does not rely on stepwise sequence processing or fixed receptive fields, thus exhibiting significant advantages in parallel computation and global information capture. However, the computational complexity of the standard self-attention mechanism increases quadratically with sequence length, making it prohibitively expensive for long-sequence tasks. In theory, the computational cost for a standard transformer is $O\left(N^2, \cdot d\right)$, where N is the sequence length and d represents the hidden dimension. In this study, as N expands to 1400, the resulting quadratic growth leads to substantial increases in attention computation, memory consumption, and runtime. Various solutions have been proposed to tackle these challenges, and among them, Linformer provides a particularly practical approach by applying a low-rank approximation to the key and value matrices, reducing complexity from $O\left(N^2\right)$ to $O(N)$ (Wang et al., 2020). Crucially, Linformer preserves the capacity for global dependency modeling while significantly cutting down on memory and computation, thereby enhancing the feasibility of transformers for long-sequence processing.

Compared to other alternatives that aim to mitigate quadratic complexity, such as sparse transformers (Child et al., 2019), Performer (Choromanski et al., 2020), and Longformer (Beltagy et al., 2020), Linformer offers a cleaner and more generally applicable solution. Sparse transformers address complexity by focusing on a limited set of positions, while Longformer and Performer rely on specialized patterns or kernel approximations. In contrast, Linformer's linear projection of keys and values provides a more straightforward, theoretically grounded method that maintains a full global receptive field (Wang et al., 2020). This simplicity and universality, free from windowed constraints or complex kernel functions, make Linformer a more practical and versatile choice for this study, ensuring that the benefits of transformers can be realized without incurring prohibitive computational and memory costs.

Building on the above optimizations, the proposed hybrid Linformer-CNN integrates one-dimensional (1D) convolutional layers (Conv1D), locally connected layers, Linformer-based self-attention, and fully connected layers to achieve a balance between feature extraction quality and computational efficiency. Specifically, Conv1D layers effectively capture local patterns within the input sequence, while locally connected layers – unlike standard convolutions – do not share weights across the entire input, thereby providing flexible mapping capabilities suitable for more fine-grained local patterns (Taigman et al., 2014). Incorporating Linformer self-attention allows the model to efficiently model long-range dependencies at linear complexity (Vaswani et al., 2017; Wang et al., 2020). Finally, the fully connected layers transform the integrated features nonlinearly, enabling hybrid Linformer-CNNs to achieve robust global contextual understanding and resource-efficient performance, thus presenting a promising architectural choice for long-sequence tasks.

On the other hand, the accuracy of surrogate models heavily depends on the quality of the finite element simulations used for training. Traditional finite element methods (FEMs) often encounter accuracy and convergence issues, particularly in the context of limit analysis of slope stability. The node-based smoothed FEM (NS-FEM) addresses these limitations by smoothing the strain field within elements, thereby reducing numerical errors and enhancing solution quality (Liu et al., 2006, 2007; Liu and Trung, 2016). In particular, the newly developed mixed formulation of limit analysis (MFLA) based on NS-FEM offers significant advantages in solving slope stability problems (Nguyen, 2023; Nguyen et al., 2025a). Prior contributions (Nguyen, 2021a, 2023; Nguyen and Vo-Minh, 2022a; Vo-Minh and Nguyen, 2022; Nguyen et al., 2025a) demonstrate that NS-FEM effectively mitigates discontinuities and oscillations commonly encountered in standard FEMs, resulting in more accurate stress and deformation predictions. Moreover, NS-FEM facilitates faster convergence of numerical solutions, reducing both computational time and effort. In the context of limit analysis, NS-FEM provides more reliable estimates of slope stability and demonstrates reduced sensitivity to mesh quality and density.

In addition, we propose a newly smoothed sequential limit analysis (SSLA) based on the Hellinger-Reissner functional for post-failure analyses of downward progressive landslides. One significant advantage of this sequential limit analysis is its ability to determine the failure pattern and corresponding FoS value at a specific mesh phase of the progressive landslides by solving optimization problems within the framework of mixed formulation limit analysis (Nguyen, 2023; Nguyen et al., 2025a). In our SSLA framework, we integrate the strengths of both mesh-based and particle approaches. The computational domain is discretized into two independent components: a set of finite elements and a set of particles. The finite elements act as a temporary tool for solving governing equations for which rigorous mathematical formulations have been established. Concurrently, the particles are utilized to store history variables and establish equilibrium equations for the subsequent computational cycle. By solving the mathematical optimization (Nguyen, 2023; Nguyen et al., 2025a), we obtain both stress and displacement fields. These updated particle positions facilitate the generation of new triangle meshes using Delaunay triangulation (Zhang et al., 2023; 2024a). The boundaries of the computational domains are identified using alpha-shape techniques (Onate et al., 2011; Zhang et al., 2013, 2014). As a result, the finite element mesh can be adjusted wholly or arbitrarily regenerated when it becomes distorted, without the need for global variable mapping during these processes. Although our framework effectively captures the post-failure patterns of slopes under certain plasticity and large deformation conditions, it is essential to note that it currently has limitations regarding the analysis of the terminal runout distance of landslides due to the absence of inertial forces in the governing equations.

Fang et al. (2023) conducted a study using a centrifuge modeling test, which is a crucial tool in understanding the deformation and failure behaviors of landslides. Including inertial forces associated with the increasing speed of soil structures during progressive landslides might capture the terminated runout distance more accurately. Centrifuge modeling can provide valuable data to validate the new numerical scheme, and dynamic parameters can be adjusted to enhance its robustness. In particular, the elastic deformation should be ignored in the dynamic elastoplastic framework given by Wang et al. (2021a) to form the SSLA based on the θ-method (Bathe and Wilson, 1972). In short, the current framework of SSLA is based on the Hellinger-Reissner variational principle, which is a form for quasistatic elastoplastic problems. Efforts should be devoted to reformulating the governing equations for dynamic elastoplastic problems (Zhang et al., 2023a; 2024b; Agbaje et al., 2024) for landslide analysis.

The main objective of this research is to evaluate the robustness of data-driven surrogate models using various ML algorithms (i.e. CNNs, fully connected networks (FCNs), and LCNs) for probabilistic analysis of slope stability in spatially variable soils. The effectiveness of the surrogate models is benchmarked through two case studies: one addressing static slope stability and the other focusing on seismic slope stability. The results reveal that the high-fidelity surrogate models, built on reliable NS-FEM analysis data, can generate statistical insights into slope stability within minutes, providing a time-efficient and, most importantly, reliable

evaluation process. Key findings highlight the potential of surrogate models utilizing various DL algorithms as valuable tools in geotechnical engineering design, particularly in scenarios involving spatially variable soils. This paper is structured as follows. Section 2 provides a methodology in which MFLA coupled with DL surrogate models using various ML algorithms (i.e., FCNs, CNNs, and LCNs) is presented for the stability analysis of spatially variable slopes. In particular, an MFLA is outlined for stochastic simulations of slope stability with spatially random soils. Subsequently, various DL algorithms (i.e. FCNs, CNNs, and LCNs) are proposed for building data-intelligent surrogate models that replace stochastic simulations of spatially variable slope stability. Section 3 validates the numerical analysis of slope stability using MFLA based on nodal integrations, showcasing its efficacy in determining slope stability. Section 4 presents numerical analysis and DL surrogate models for the stability of spatially variable slopes, where data-intelligent surrogate models are built using FCNs, CNNs, and LCNs. Some of the highlighted features of the use of DL surrogate models for the stability analysis of spatially variable slopes are summarized in Section 5.

2. Methodology

This section presents a numerical framework that integrates a newly developed SSLA with the multi-downsampling hybrid Linformer-CNN model to analyze the stability of spatially variable slopes. Firstly, we introduce a newly developed numerical framework of an SSLA tailored explicitly for large-deformation slope analysis. The newly developed numerical procedure is based on the stress-based upper-bound (UB) limit analysis theory (Nguyen, 2023; Nguyen et al., 2025a), which is crucial for determining the limit state of a given geometry. Subsequently, we detail how the displacements of nodes are utilized to update the mesh. We retain only the number of nodes to mitigate mesh distortions, ignoring the triangle elements in the next step. Using the alpha-shape technique (Zhang et al., 2013, 2014, 2021), the updated particle positions are then employed to generate new triangle meshes. A key advantage of SSLA is that it preserves and updates all properties at the nodes from the previous step. Importantly, at any given step or for a specific geometry, extracting the positions of nodes and calculating the FoS is a straightforward process. Next, we introduce the development of the multi-downsampling hybrid Linformer-CNN model, which employs parallel multi-scale CNN branches with distinct pooling strategies, followed by Linformer-based self-attention layers (Wang et al., 2020) to effectively capture both local and global dependencies within the data. Utilizing a dataset generated from numerical simulations, this hybrid model serves as a DL surrogate to accurately predict FoS values. Fully connected layers are used to integrate and refine the combined multi-scale features, enhancing the model's predictive capability. By leveraging the strengths of CNNs for local feature extraction and Linformer layers for efficient global dependency modeling, the multi-downsampling hybrid Linformer-CNN framework provides a robust and scalable approach for slope stability analysis under complex geotechnical conditions.

2.1. A newly developed SSLA based on the Hellinger-Reissner functional using NS-FEM

Considering the medium Ω, which is bounded by the displacement boundary $\Omega_{\boldsymbol{u}}$ and the stress boundary Ω_{σ}, we analyze the effects of applying tractions t on the traction boundary $\Gamma_{\boldsymbol{t}}$. In this context, $\boldsymbol{u}$ and $\boldsymbol{\sigma}$ denote the displacement and stress fields, respectively. Additionally, $\boldsymbol{b}$ represents the body force, while $\boldsymbol{t}$ signifies the traction force, as shown in Fig. 1. The Hellinger-

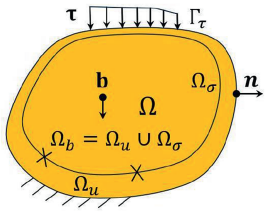

Fig. 1. Medium Ω with boundary $\Omega_b = \Omega_{\boldsymbol{u}} \cup \Omega_{\sigma}$ subjected to tractions $\boldsymbol{t}$ on $\Gamma_{\boldsymbol{t}}$ and support on $\Omega_{\boldsymbol{u}}$ (OptumCE, www.optumce.com).

Reissner functional (Krabbenhøft et al., 2005, 2007, 2012; Krabbenhøft, 2009) for perfect plastic materials is expressed as follows:

$$\pi(\boldsymbol{u},\boldsymbol{\sigma}) = \int_{\Omega} \boldsymbol{\sigma}\nabla\boldsymbol{u}\mathrm{d}\Omega - \int_{\Omega} \boldsymbol{b}^{\mathrm{T}}\Delta\boldsymbol{u}\mathrm{d}\Omega - \int_{\Gamma_{\boldsymbol{t}}} \boldsymbol{t}^{\mathrm{T}}\Delta\boldsymbol{u}\mathrm{d}\Gamma_{\boldsymbol{t}} \tag{1}$$

where ∇ is the linear strain–displacement differential operator.

The boundary-value problem (Eq. (1)) can be formulated as a max-min problem given by

$$\underbrace{\min}_{\boldsymbol{u}}\ \underbrace{\max}_{\boldsymbol{\sigma}} \int_{\Omega} \boldsymbol{\sigma}\nabla\boldsymbol{u}\mathrm{d}\Omega - \int_{\Omega} \boldsymbol{b}^{\mathrm{T}}\Delta\boldsymbol{u}\mathrm{d}\Omega - \int_{\Gamma_{\boldsymbol{t}}} \boldsymbol{t}^{\mathrm{T}}\Delta\boldsymbol{u}\mathrm{d}\Gamma_{\boldsymbol{t}} \tag{2}$$

subjected to

$$F(\boldsymbol{\sigma}) \le 0 \tag{3}$$

In accordance with standard FEM (see Fig. 2a), the MFLA based on the variational Hellinger-Reissner functional (Nguyen, 2023; Nguyen et al., 2025a) can be expressed as

$$\underbrace{\min}_{\hat{\boldsymbol{u}}}\ \underbrace{\max}_{\bar{\sigma}} \left(\alpha + \boldsymbol{\sigma}^{\mathrm{T}}\boldsymbol{B}\boldsymbol{u} - \alpha\boldsymbol{p}^{\mathrm{T}}\boldsymbol{u} - \boldsymbol{p}_0^{\mathrm{T}}\boldsymbol{u}\right) \tag{4}$$

subjected to

$$\left.\begin{array}{l} \boldsymbol{B}^{\mathrm{T}}\boldsymbol{\sigma} = \alpha\boldsymbol{p} + \boldsymbol{p}_0 \\ F(\boldsymbol{\sigma}) \le 0 \end{array}\right\} \tag{5}$$

where α is the load multiplier; $\boldsymbol{B} = \int_{\Omega} \boldsymbol{N}_{\boldsymbol{\sigma}}^{\mathrm{T}}\boldsymbol{B}_{\boldsymbol{u}}\mathrm{d}\Omega$; $\boldsymbol{p} = \int_{\Omega} \boldsymbol{N}_{\boldsymbol{u}}^{\mathrm{T}}\boldsymbol{b}\mathrm{d}\Omega + \int_{\Gamma_{\boldsymbol{t}}} \boldsymbol{N}_{\boldsymbol{u}}^{\mathrm{T}}\boldsymbol{t}\mathrm{d}\Gamma_{\boldsymbol{t}}$; and $\boldsymbol{p}_0 = \int_{\Omega} \boldsymbol{N}_{\boldsymbol{u}}^{\mathrm{T}}\boldsymbol{b}_0\mathrm{d}\Omega + \int_{\Gamma_{\boldsymbol{t}}} \boldsymbol{N}_{\boldsymbol{u}}^{\mathrm{T}}\boldsymbol{t}_0\mathrm{d}\Gamma_{\boldsymbol{t}}$; $\boldsymbol{N}_{\sigma}$ and $\boldsymbol{N}_{\boldsymbol{u}}$ are the matrices of shape functions; $\boldsymbol{B}_{\boldsymbol{u}}$ is the strain gradient matrix of the linear triangular elements; and $\boldsymbol{p}$ and $\boldsymbol{p}_0$ are the vectors of optimizable and given forces, respectively.

In the context of the MFLA using NS-FEM (Nguyen, 2023; Nguyen et al., 2025a), the computational domain is segmented into elements similar to the traditional FEM. A distinguishing feature of the MFLA using NS-FEM is its application of smoothing

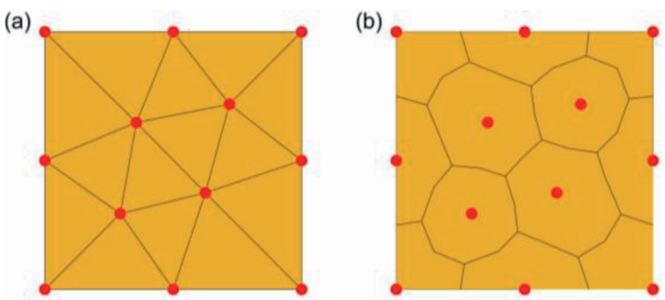

Fig. 2. Typical meshes: (a) Standard FEM; and (b) MFLA using NS-FEM.

operations to the strain field over subdomains linked to individual nodes, which leads to solutions that are significantly more stable and accurate than those obtained through conventional FEM. Furthermore, while the MFLA in standard FEM (Krabbenhøft et al., 2005; Krabbenhoft and Lyamin, 2012) typically relies on approximating two master fields based on individual elements, MFLA with NS-FEM determines these unknown variables using the smoothing domains surrounding the nodes. In this numerical framework, which incorporates NS-FEM and second-order cone programming (SOCP), the equilibrium conditions and yield criteria are established on the smoothing domains rather than at Gauss points, as is customary in FEM. Both stress and strain are treated as constant across these nodal smoothing domains. As a result, the numerical framework for MFLA employing NS-FEM (as illustrated in Fig. 2b) is formulated as follows:

$$\underbrace{\min}_{\widehat{\boldsymbol{u}}}\ \underbrace{\max}_{\overline{\boldsymbol{\sigma}},\alpha}\ \left(\alpha+\overline{\boldsymbol{\sigma}}^{\mathrm{T}}\boldsymbol{B}\widehat{\boldsymbol{u}}-\alpha\boldsymbol{p}^{\mathrm{T}}\widehat{\boldsymbol{u}}-\boldsymbol{p}_0^{\mathrm{T}}\widehat{\boldsymbol{u}}\right) \tag{6}$$

subjected to

$$\left.\begin{array}{l}\boldsymbol{B}^{\mathrm{T}}\overline{\boldsymbol{\sigma}}=\alpha\boldsymbol{p}+\boldsymbol{p}_0\\ F(\overline{\boldsymbol{\sigma}})\le 0\end{array}\right\} \tag{7}$$

where $\boldsymbol{B}=\int_{\Omega}\boldsymbol{N}_{\sigma}^{\mathrm{T}}\overline{\boldsymbol{B}}\mathrm{d}\Omega$.

The stress in the smoothing cells surrounding nodes within the NS-FEM framework is expressed as a function of $\widehat{\boldsymbol{\sigma}}$, the vector of stress components at the mesh nodes. This relationship can be approximated by

$$\boldsymbol{\sigma}\approx\boldsymbol{N}_{\sigma}\widehat{\boldsymbol{\sigma}}\approx\boldsymbol{N}_{\sigma}\overline{\boldsymbol{\sigma}} \tag{8}$$

where $\overline{\boldsymbol{\sigma}}$ represents the vector of stress components within the cell, given that $\overline{\boldsymbol{\sigma}}=\boldsymbol{\sigma}$. In this context, $\boldsymbol{N}_{\sigma}$ serves as an identity matrix.

Similarly, the displacement $\widehat{\boldsymbol{u}}$ is approximated over a three-node triangular element as follows:

$$\boldsymbol{u}\approx\boldsymbol{N}_{\boldsymbol{u}}\widehat{\boldsymbol{u}} \tag{9}$$

where $\widehat{\boldsymbol{u}}$ is the vector of displacement components at the mesh nodes.

The strain in each smoothing domain (i.e. Ω_k^{s}) is estimated as a weighted average of the strain from all the one-third elements adjacent to the node. This can be expressed as

$$\overline{\boldsymbol{\epsilon}}_k=\frac{1}{A_k^{\mathrm{s}}}\sum_{i=1}^{N_{\mathrm{s}}}\frac{1}{3}A_i^{\mathrm{e}}\boldsymbol{\epsilon}_i^{\mathrm{e}}=\overline{\boldsymbol{B}}_k\widehat{\boldsymbol{u}}_i^{\mathrm{e}} \tag{10}$$

where $\overline{\boldsymbol{B}}_k$ is defined as

$$\overline{\boldsymbol{B}}_k=\frac{1}{A_k^{\mathrm{s}}}\sum_{i=1}^{N_{\mathrm{s}}}\frac{1}{3}A_i^{\mathrm{e}}\boldsymbol{B}_i^{\mathrm{e}} \tag{11}$$

where i denotes the number of the adjacent element; A_k^{s} represents the area of the smoothing cell associated with node k (i.e. $A_k^{\mathrm{s}}=\frac{1}{3}\sum_{i=1}^{N_{\mathrm{s}}}A_i^{e}$); N_{s} is the total number of adjacent elements for each cell; and A_i^{e}, $\boldsymbol{\epsilon}_i^{\mathrm{e}}$, $\boldsymbol{B}_i^{\mathrm{e}}$, and $\widehat{\boldsymbol{u}}_i^{\mathrm{e}}$ refer to the area, strain, strain gradient matrix, and displacement of the ith triangular element, respectively. Consequently, the strain over the cell can be computed as

$$\overline{\boldsymbol{\epsilon}}=\nabla\boldsymbol{u}=\overline{\boldsymbol{B}}\widehat{\boldsymbol{u}} \tag{12}$$

For plane-strain problems, the Mohr-Coulomb yield criterion, which depends on the parameters of cohesion c and the friction angle φ, is utilized. This yield criterion is applied to all nodal smoothing cells, and is expressed as follows:

$$F(\overline{\boldsymbol{\sigma}})=\sqrt{\left(\overline{\sigma}_{xx}-\overline{\sigma}_{yy}\right)^2+4\overline{\tau}_{xy}^2}+\left(\overline{\sigma}_{xx}+\overline{\sigma}_{yy}\right)\sin\varphi-2c\cos\varphi\le 0 \tag{13}$$

A new variable, $\boldsymbol{\rho}$, is introduced into the inequality condition as the set of conic constraints as follows:

$$\boldsymbol{\rho}=\begin{bmatrix}\rho_1\\ \rho_2\\ \rho_3\end{bmatrix}=\boldsymbol{D}\overline{\boldsymbol{\sigma}}+\boldsymbol{d}=\begin{bmatrix}-\sin\varphi & -\sin\varphi & 0\\ 1 & -1 & 0\\ 0 & 0 & 2\end{bmatrix}\begin{bmatrix}\overline{\sigma}_{xx}\\ \overline{\sigma}_{yy}\\ \overline{\tau}_{xy}\end{bmatrix}+\begin{bmatrix}2c\cos\varphi\\ 0\\ 0\end{bmatrix} \tag{14}$$

The inequality condition is defined as a cone constraint (Nguyen, 2023; Nguyen et al., 2025a):

$$\mathscr{K}_q=\left\{\boldsymbol{\rho}\in\mathbb{R}^3\middle|\rho_1\ge\sqrt{\rho_2^2+\rho_3^2}\right\} \tag{15}$$

The MFLA (as expressed in Eq. (6)) is formulated as a SOCP problem:

$$FoS=\underbrace{\max}_{\overline{\boldsymbol{\sigma}},\alpha}\ \alpha=\underbrace{\max}_{\overline{\boldsymbol{\sigma}},\alpha}\ \boldsymbol{a}^{\mathrm{T}}\boldsymbol{X} \tag{16}$$

subjected to

$$\left.\begin{array}{l}\boldsymbol{A}_{\mathrm{eq}}\boldsymbol{X}=\boldsymbol{b}_{\mathrm{eq}}\\ \boldsymbol{X}\in\mathscr{K}\end{array}\right\} \tag{17}$$

where $\boldsymbol{X}$ denotes the stress and displacement fields formulated as cone constraints, such that $\boldsymbol{X}\in\mathscr{K}$ (Nguyen, 2023; Nguyen et al., 2025a, 2025b). We coded the framework in MATLAB, formulating the MFLA based on the Hellinger-Reissner variational principle as a mathematical optimization problem with cone constraints. To solve the optimization problem, the conic interior-point optimizer from the MOSEK academic package (MOSEK ApS, 2015) was employed. For instance, Fig. 3 displays typical mesh configurations and boundary conditions for a slope, showcasing FEM (Fig. 3a) and NS-FEM (Fig. 3b) approaches. Notably, while the framework of MFLA using NS-FEM and SOCP builds upon FEM meshes, the unknown variables are defined at the nodal smoothing cells rather than within the elements. The FoS value, represented as α, is computed directly by solving the SOCP problem, as outlined in Eqs. (16) and (17). For further details regarding the solution scheme for the SOCP problem, readers are encouraged to

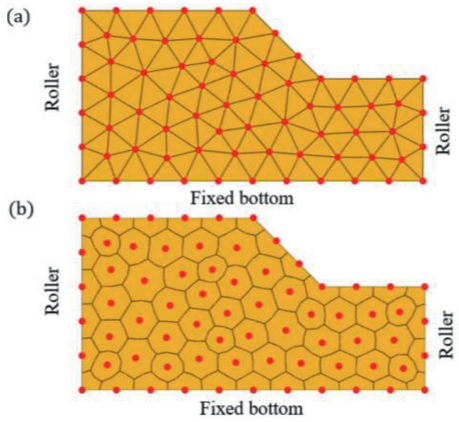

Fig. 3. The typical mesh configurations and boundary conditions for a slope using: (a) Standard FEM; and (b) MFLA using NS-FEM.

consult previous studies (Nguyen, 2023; Nguyen et al., 2024b, 2025a, b).

As can be observed in the mathematical optimization (Eqs. (16) and (17)), the final form of the Hellinger-Reissner variational principle is framed as a min-max optimization problem with conic constraints. The numerical scheme's principle is to solve the mathematical optimization problem to get both stress and displacement fields. Here, two master fields are stored at nodes. We neglect the mesh of the previous computation cycles and just keep the updated nodes, where the positions of the nodes are upgraded using the displacement fields. The new mesh is generated based on the cloud of updated nodes instead of keeping the old meshes, where the updated position of nodes can lead to severe mesh distortion, especially along the shear band where failure is formed. In particular, the updated particle positions are employed to generate new triangle meshes via Delaunay triangulation. Following this, we utilize the alpha-shape technique to redefine the boundaries of the computational domain by removing unnecessary meshes. The fundamental concept of the alpha-shape method operates as follows. Considering a set of points distributed in space, which are characterized by a separation distance denoted as h, for a given parameter α_{sh}, any point situated on an empty sphere with a radius exceeding α_{sh} times the characteristic spacing (i.e. $\alpha_{\mathrm{sh}}h$) is identified as a boundary node. In other words, for each point within the dataset, we analyze whether it is possible to position a sphere of radius $\alpha_{\mathrm{sh}}h$ such that it encompasses only that particular point. If this is successful, the point qualifies as a boundary point; if the sphere encompasses more than one point, the point is classified as an internal point.

In this study, the value of h is chosen as the mean circumradius of the triangles generated through Delaunay triangulation. Triangles with a circumcircle radius greater than $\alpha_{\mathrm{sh}}h$ are deleted, indicating that the computational domain is highly sensitive to the value of α_{sh}. Previous numerical reports by Zhang et al. (2013, 2014) indicate that the identification of computational domains is significantly influenced by the α_{sh} value. Numerical studies (Onate et al., 2011; Zhang et al., 2013, 2014) suggest that a value of α_{sh} slightly greater than 1 is appropriate and aligns with practical applications. For instance, for a wide range of coupled fluid–solid interaction problems, Onate et al. (2011) concluded that a value of α_{sh} in the range of 1.3–1.5 is suitable. In this study, we find the optimal range of α_{sh} to be approximately 1.4–1.6. Fig. 4 illustrates the identification of computational domains for various α_{sh} values. Specifically, Fig. 4b demonstrates that $\alpha_{\mathrm{sh}} = 1.5$ is the most suitable value for defining new computation domains using the alpha-shape method in the subsequent cycle.

Moreover, we could include two general techniques in the numerical schemes to deal with the potential instability associated with the new meshes' dependencies on the chosen α_{sh} value. First, we need to identify the triangle elements with a circumcircle radius greater than $\alpha_{\mathrm{sh}}h$. Next, we further add either (1) a node at the centre of the triangle element (technique 1) or (2) a node on the longest edge of the triangle element (technique 2). These techniques involve adding new nodes to the cloud of existing nodes, which are then used to generate a new mesh through Delaunay triangulation. The computation domain is then identified using the alpha-shape technique with $\alpha_{\mathrm{sh}} = 1.5$. These techniques mitigate the potential instability of sensitivity analysis by identifying the computational domain using the alpha-shape technique.

To summarize, the entire computational cycle of the sequential limit analysis is illustrated in Fig. 5. A critical issue in each step is identifying the computational domain based on the updated cloud of points. The primary advantage of the SSLA is that it preserves and updates all properties at the nodes from the previous step, eliminating the need for variable mapping. The use of low-order elements enhances the computational efficiency of the numerical scheme. This proposed numerical approach, combined with an updated geometry, is well-suited for simulating large deformations. Furthermore, the integration of MFLA with particle characteristics, inherited from the particle FEM framework, facilitates the study of progressive slope failure.

Following Nguyen (2023), 1000 samples of seismic accelerations are generated to assess the effect of seismic forces on FoS values. Horizontal (α_{h}) and vertical (α_{v}) seismic accelerations are random vectors generated by the quasi-random sequence, as shown in Fig. 6, where the magnitude of α_{h} and α_{v} varies from 0 to 0.5. Herein, the FoS value is a function of spatially variable soil properties and seismic accelerations (i.e. $\mathrm{FoS}(\chi) = f(c(x), \varphi(x), \alpha_{\mathrm{h}},$

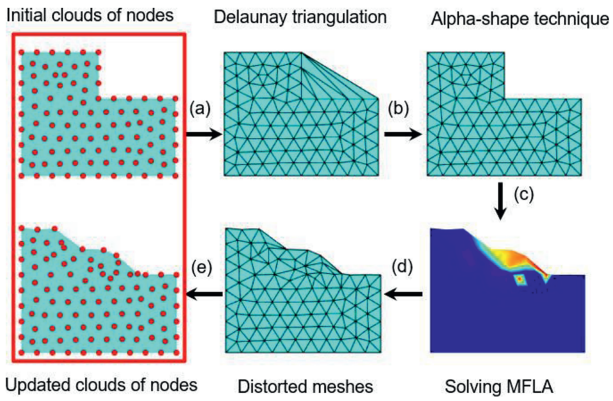

Fig. 5. Computational cycles of the sequential limit analysis: (a) Cloud of particles with meshes generated by Delaunay triangulation at step n; (b) Triangular elements obtained from the alpha-shape method at step n; (c) Solving equations to determine the FoS; (d) Updated deformed mesh at step $n+1$; and (e) Updated particle positions at step $n+1$ for generating new meshes.

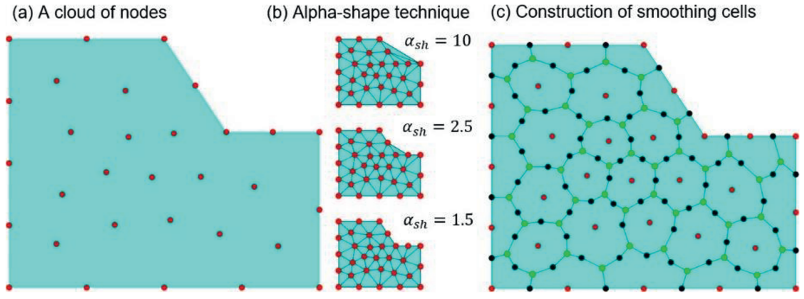

Fig. 4. Generation of nodal smoothing cells: (a) A cloud of particles; (b) Meshes generated by Delaunay triangulation and identification of the computational domain using the alpha-shape method; and (c) Construction of smoothing cells for MFLA.

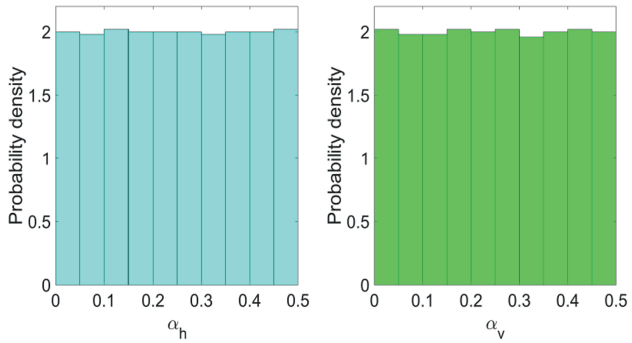

Fig. 6. Quasi-randomly generated horizontal (α_h) and vertical (α_v) seismic accelerations for FoS calculations in the probabilistic framework.

α_v), where $c(x)$ and $\phi(x)$ are the spatial random fields and $\boldsymbol{x}$ is denoted as the spatial coordinate. The numerical scheme adopts the pseudo-static approach (Nguyen and Vo-Minh, 2022a, b; Nguyen, 2023) for seismic acceleration, in which the equivalent seismic forces are treated as additional loads acting on soil. In particular, the horizontal seismic acceleration results in extra static forces, which are proportional to the soil weight and the horizontal seismic acceleration values. Integrating such extra forces into the body forces in the numerical procedure is straightforward. A similar procedure is applied to vertical seismic accelerations. The pseudo-static approach, with its simplicity and efficiency, plays a key role in assessing seismic stability. However, its reliability can vary considerably based on the purpose for which it is applied. It can be appropriate for less critical structures or during early design phases. For high-risk applications or complex structures, more accurate dynamic analysis methods are recommended to ensure safety and performance. This is because the pseudo-static approach does not capture the time history of seismic accelerations, which can significantly influence the soil responses and properties during an earthquake.

2.2. Overview of DL surrogate models for slope stability analysis

In the evolution of ML and DL, numerous advanced algorithms and architectures have been successfully applied across various scientific and engineering domains. Early studies (Goh, 1994a, b, 1995a, b, Goh, 1996) introduced ANNs into geotechnical engineering, providing novel solutions for predicting soil and rock mechanical behavior and stability. As computational power and algorithmic sophistication have improved, a wider range of ML methods, including SVMs, ANN variants, and random forests, have been employed to tackle increasingly complex geotechnical problems (Byvatov and Schneider, 2003; He et al., 2020; Baghbani et al., 2022; Zhang et al., 2022). More recently, DL techniques such as CNNs, RNNs, transformers, and emerging attention mechanisms have provided highly efficient, flexible, and data-driven modeling tools for geotechnical applications (LeCun et al., 2015; Vaswani et al., 2017).

In this study, we propose a hybrid DL framework for predicting slope stability. Slope stability analysis typically relies on finite element simulations and random field generation, where the input data encompass spatially varying soil parameters such as cohesion (c), friction angle (φ), and unit weight (γ). These parameters are often sampled over complex, irregular domains discretized by FEMs. Unlike regular grids (e.g. uniform two-dimensional (2D) pixel arrays or three-dimensional (3D) voxels), finite element meshes yield irregular nodal distributions governed by complex topography and geological heterogeneity. Tools like GSTools (Müller et al., 2022) can generate unstructured random fields, assigning soil strength parameters ($c, \varphi,$ and γ) to each finite element node without forming a regular spatial tensor suitable for direct application of 2D or 3D convolutions.

In this study, we use the random Fourier discrete model (RFDM) to generate random fields. The RFDM represents a spatially variable field as a sum of sinusoidal components. This approach is advantageous because it allows for a flexible and efficient representation of spatial correlations between points in the field. The random field is generated by defining a spectral density function $S(k)$, which controls the correlation properties. The spectral density function is typically specified by a power spectrum parameterized by the correlation length and possible anisotropy. These parameters determine how quickly properties change across space and in specific directions. The Fourier coefficient $\widehat{f}$ is then derived from this spectral function, allowing the random field to be reconstructed as

$$f(x) = \sum_k \widehat{f}(k) \mathrm{e}^{ikx} \tag{18}$$

where k is the wavevector corresponding to the spatial frequency. The RFDM ensures that the random field maintains continuous spatial variability while accurately reflecting real-world geological conditions. By using this model, multiple realizations of the random field can be generated, capturing the uncertainty in the geotechnical parameters such as cohesion and friction angle. These realizations are then used to create training datasets for ML models, enabling the prediction of slope stability under various conditions.

The uncertainty in the input data propagates through the DL model in three primary ways. First, the input soil parameters (e.g. cohesion, friction angle, and unit weight) are generated as spatially variable random fields, with each parameter explicitly modeled by a log-normal distribution defined by its mean, standard deviation, and correlation length, capturing its inherent uncertainty. Second, due to the stochastic nature of these inputs, the model learns the complex relationships between spatially variable features and the FoS during training, resulting in a distribution of predictions rather than a single deterministic value. Third, the predictions exhibit uncertainty owing to factors such as limited training data, model architecture, and optimization processes.

A common strategy to handle such irregular data is to 'linearize' it. In this approach, the parameter values at each finite element node are arranged into a 1D sequence according to a predefined ordering rule. In this work, we adopt an index-based ordering method, leveraging the node numbering from the preprocessing step of the finite element model. By sequentially concatenating the parameter values following the node indices, we transform the inherently irregular spatial data into a 1D vector of length N, where N is the total number of nodes. Although this linearization weakens the explicit spatial adjacency encoded in 2D or 3D structures, CNN1D and attention mechanisms can still capture local dependencies along the sequence. In essence, while this representation cannot fully preserve the original spatial neighborhood relationships, applying Conv1D filters along the sequence allows us to approximate local patterns and, to some extent, reflect the underlying spatial correlations in a 1D format. Various network architectures exhibit distinct advantages in handling different data structures and tasks. FCNs represent one of the most fundamental architectures, connecting every neuron in one layer to all neurons in the next (Sakellariou and Ferentinou, 2005). According to the universal approximation theorems, one-hidden-layer FCNs can fit any complex nonlinear equation, as long as sufficient neurons are given (Hornik et al., 1989). However, the

general connection makes FCN less efficient in extracting spatial or temporal features. In contrast, CNNs excel at capturing local structure by applying convolutional kernels over the input data (Krizhevsky et al., 2017; Gu et al., 2018). For 1D data, such as time series, signal processing outputs, or linearly mapped geotechnical parameters, CNN1D utilizes sliding kernels to extract local patterns and spatial correlations between adjacent input data (Krizhevsky et al., 2017). However, local convolutions alone may be insufficient to model long-range dependencies. To address this, transformer-based attention mechanisms have emerged, demonstrating remarkable success in capturing global context by assigning weights to relationships between all pairs of positions in a sequence (Vaswani et al., 2017). The classical transformer incurs $O\left(N^2\right)$ complexity in sequence length, raising computational costs for large inputs. Linformer, a variant of the transformer, tackles this challenge by applying low-rank approximations to the attention matrix, effectively reducing time and memory complexity (Wang et al., 2020). This allows global dependency modeling to remain tractable for longer sequences.

Our proposed multi-downsampling hybrid Linformer-CNN model fundamentally differs from these conventional approaches in several key aspects. First, by integrating both AveragePooling1D and MaxPooling1D layers in parallel, our method performs multi-scale feature extraction that captures both mid-level and coarse-grained global features – a capability not typically addressed by standard CNNs or FCNs. Second, the incorporation of Linformer-based self-attention layers after the downsampling steps enables efficient modeling of long-range dependencies while keeping computational costs low. This hybrid architecture bridges the gap between local feature extraction and global contextual understanding, specifically tailored to address the challenges of irregular geotechnical data.

In this research, we integrate and compare multiple architectures – FCN, CNN1D, and Linformer self-attention – within a single hybrid model. FCN provides a baseline for nonlinear mapping between input and output, CNN1D enhances local feature extraction within the 1D sequences, and Linformer self-attention efficiently captures long-range global dependencies. To further strengthen the model's capacity to represent multi-scale features, we design a multi-scale downsampling strategy, enabling the simultaneous extraction of different feature levels:

(1) Two AveragePooling1D (i.e. pool size = 2) layers produce a medium-resolution representation, capturing mid-level features.
(2) Two MaxPooling1D (i.e. pool size = 4) layers yield a low-resolution representation, focusing on coarser-scale, global patterns.

By integrating these multi-resolution features, our hybrid model can simultaneously exploit both local and global characteristics of the input data. After processing through FCN, CNN1D, and Self-determination layers, the combined model outputs a prediction of the FOS for slope stability. Throughout training, weights and biases are adjusted via back-propagation to minimize prediction errors, and model performance is validated against separate test datasets to ensure generalization.

2.2.1. FCN

FCNs (Gurney, 2018) constitute one of the most fundamental architectures in neural network design, distinguished by their straightforward and comprehensive connectivity. In FCNs, each neuron within a hidden layer is connected to every neuron in the adjacent layer, forming what are commonly referred to as 'dense layers'. This extensive interconnectivity enables FCNs to model complex and nonlinear relationships between input and output variables effectively. The learning process in FCNs involves forward propagation, where input data are sequentially processed through each layer, and backpropagation, where the network iteratively adjusts its weights based on the error between predicted and actual outputs. Despite their flexibility, FCNs are limited by their inability to capture spatial structures and local dependencies. Additionally, dense connections may lead to high computational costs and an increased risk of overfitting, making them less suitable for tasks that require an understanding of spatial or sequential relationships.

2.2.2. CNN1D

A CNN1D extends the convolutional paradigm, originally developed for 2D images, into the temporal or sequential domain. In a CNN1D, filters (also known as kernels) slide along a single spatial or temporal dimension, extracting local features from segments of the input signal, as illustrated in Fig. 7a. Each convolutional operation produces a feature map that highlights patterns, such as changes in soil parameters along a slope profile. 1D pooling layers are followed by the 1D convolutional layers, as shown in Fig. 7b. By stacking multiple convolutional and pooling layers, the CNN1D can progressively learn hierarchical representations, starting from simple, low-level features to more complex, higher-level patterns. This makes CNN1Ds particularly well-suited for sequence-like data, as they naturally capture local correlations between adjacent input elements, leading to improved generalization compared to fully connected layers applied directly to raw data.

2.2.3. Multi-scale downsampling strategy

Integrating AveragePooling1D and MaxPooling1D layers in parallel pathways allows the model to capture features at multiple scales, which is critical for slope stability analysis. AveragePooling1D computes the mean over each pooling window, capturing the overall trends and medium-scale variations in soil properties. This provides a smoothed representation of the data, reflecting large-scale spatial variations in the slope. In contrast, MaxPooling1D selects the maximum value within each window, emphasizing local extremes that may indicate critical points of instability, such as zones of soil weakness or imminent failure.

By integrating these two pooling strategies, our model benefits from a comprehensive feature representation that balances both global trends and local details. This dual approach enhances robustness and generalization, as it reduces dependency on a single scale of information and mitigates the effects of noise and irregularities in the input data. Moreover, the pooling layers efficiently reduce the sequence length, lowering the computational burden for subsequent layers without sacrificing essential information.

2.2.4. Self-attention and Linformer for efficient attention

Transformers revolutionized sequence modeling through self-attention, which calculates interactions between every pair of positions in a sequence, enabling the capture of long-range dependencies (Vaswani et al., 2017). The self-attention can be expressed as

$$\text{Attention}(\boldsymbol{Q},\boldsymbol{K},\boldsymbol{V}) = \text{softmax}\left(\frac{\boldsymbol{Q}\boldsymbol{K}^{\mathrm{T}}}{\sqrt{d_k}}\boldsymbol{V}\right) \tag{19}$$

where d_k is the dimensionality of the key vectors in the self-attention. Fig. 8 shows calculations of $\boldsymbol{Q}$, $\boldsymbol{K}$, and $\boldsymbol{V}$ in self-attention in the transformer.

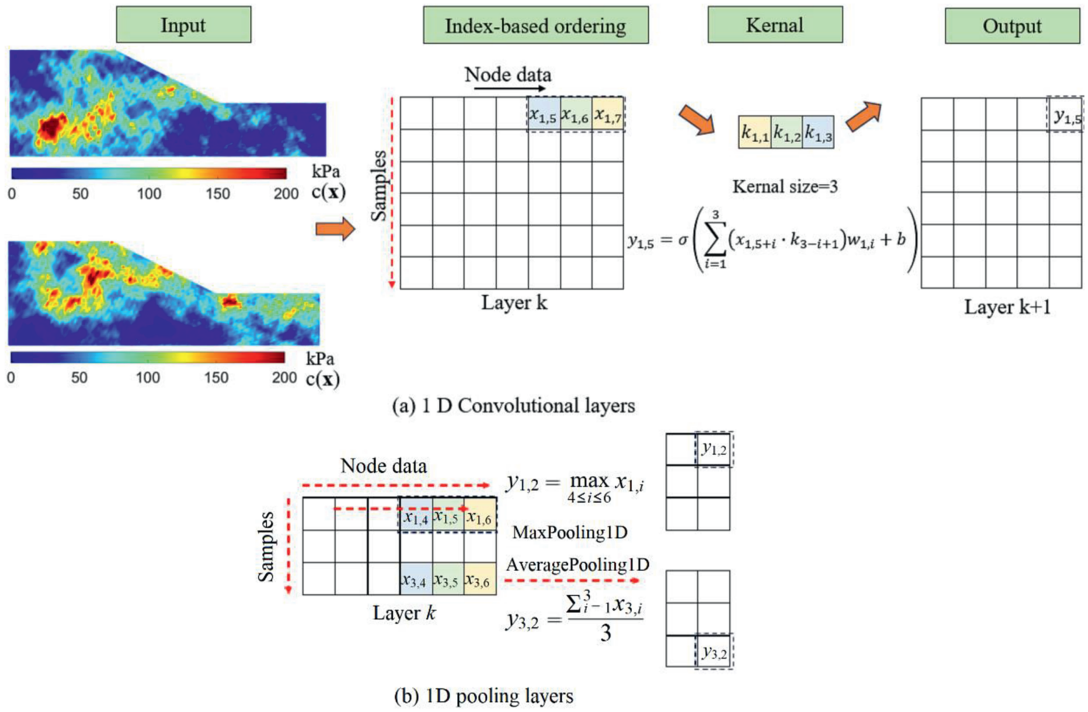

Fig. 7. Diagrams of CNN1D: (a) 1D convolutional layers; and (b) 1D pooling layers.

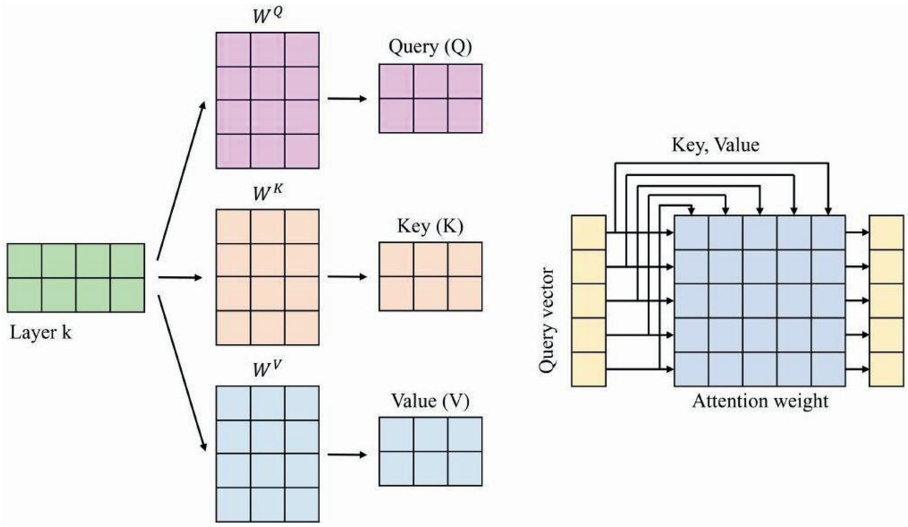

Fig. 8. *K*, ***Q***, and ***V*** calculated in the transformer.

However, the classical transformer suffers from quadratic complexity in sequence length. The core of the transformer lies in its self-attention mechanism, which computes attention scores by taking the dot product of query (***Q***) and key (***K***) matrices, scaling by the square root of the key dimension and applying a softmax function to obtain attention weights. These weights are then used to compute a weighted sum of the value (***V***) matrices. This results in a computational complexity of $O\left(N^2 d_{\text{model}}\right)$ and a memory complexity of $O\left(N^2\right)$, where N is the sequence length and d_{model} is the dimensionality of the model. Such scaling becomes prohibitive for long sequences.

Linformer (Wang et al., 2020) addresses this limitation by projecting the key-value representations into a lower-dimensional space, approximating the full attention matrix with a reduced-rank structure. Linformer can be expressed as

$$\text{Attention}(\boldsymbol{Q},\boldsymbol{K},\boldsymbol{V}) = \text{softmax}\left(\frac{\boldsymbol{Q}(\boldsymbol{EK})^{\mathrm{T}}}{\sqrt{d_k}}\boldsymbol{FV}\right) \tag{20}$$

where ***EK*** and ***F*** are the fixed projection matrices to project the key (***K***) and value (***V***) matrices from their original sequence length N to a lower dimension k. Specifically, ***EK*** can project the key ***K*** from (N, d_k) to (k, d_k) and ***FV*** can project the value ***V*** from (N, d_k) to (k, d_v), where $k \ll N$. The computational complexity then goes into $O(N)$, which is far smaller than $O\left(N^2 d_{\text{model}}\right)$. This low-rank approximation maintains most of the information necessary for

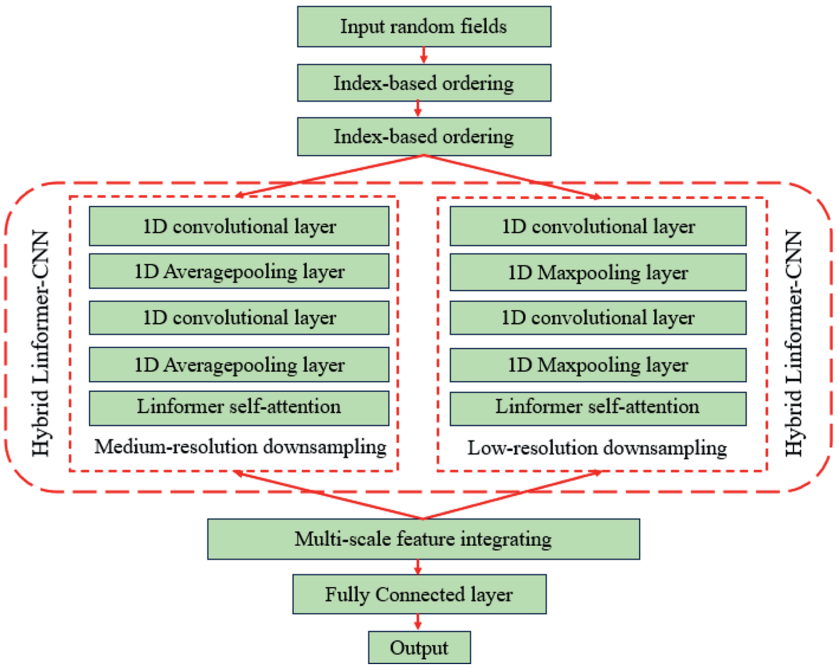

Fig. 9. The architecture of the hybrid Linformer-CNN.

effective global context modeling while substantially decreasing computational and memory costs. As a result, Linformer enables efficient handling of longer sequences, allowing our model to integrate global spatial correlations among geotechnical parameters across an extensive input domain without incurring prohibitive computational overhead. This makes Linformer-based self-attention layers a powerful component in our hybrid architecture, combining local feature extraction with efficient global feature integration.

2.3. Overview of the newly proposed multi-downsampling hybrid Linformer-CNN for slope stability prediction

In our approach, the spatially variable soil parameters are defined initially on a 2D domain and then linearized into a 1D sequence to facilitate the use of 1D convolutional (Kiranyaz et al., 2021) and self-attention mechanisms. Although this flattening process reduces the explicit representation of 2D spatial correlations, the model still learns these dependencies indirectly through the learned filters in the Conv1D layers and the attention weights in the Linformer layer. In effect, the DL architecture can capture both local and global interactions, despite the loss of an explicit 2D structure. The multi-scale downsampling strategy effectively learns shorter spatial correlation lengths to ensure robust local feature extraction, while the self-attention mechanism in the Linformer layer effectively captures long-range dependencies, thereby enhancing the model's ability to recognize global features.

In summary, the hybrid model proposed in this study achieves slope stability prediction through the following steps, as shown in Figs. 9 and 10.

2.3.1. Initial data processing

First, 1D feature sequences for cohesion (c), friction angle (φ), and unit weight (γ) are generated using random field simulations. This process linearizes the input data, which inherently possesses irregular geometric shapes, thereby converting them into a linear sequence format. This transformation facilitates the application of 1D convolutional (Kiranyaz et al., 2021) and attention mechanisms.

2.3.2. Multi-scale feature extraction

The model employs two parallel downsampling pathways to extract multi-scale features.

(1) Hybrid Linformer-CNN pathway 1 (AveragePooling path)
   (i) Conv1D layer. A 1D convolution with 32 filters and a kernel size of 3 is applied, using the ReLU activation function. This layer detects local patterns within small segments of the input sequence.
   (ii) AveragePooling1D layer. The dimensionality is reduced by averaging over a pool size of 2, effectively capturing mid-level features while retaining essential information.
   (iii) LinformerSelfAttention layer. The LinformerSelfAttention mechanism with a projection dimension $k = 256$ is applied to capture long-range dependencies efficiently within the medium-scale features.

(2) Hybrid Linformer-CNN pathway 2 (MaxPooling path)
   (i) Conv1D layer. A 1D convolution with 32 filters and a kernel size of 3 is applied, using the ReLU activation function.
   (ii) MaxPooling1D layer. This layer reduces the dimensionality by taking the maximum value over a pool size of 4, emphasizing prominent, global features.
   (iii) Conv1D layer. Another Conv1D layer with 32 filters and a kernel size of 3 further processes the coarse features.
   (iv) MaxPooling1D layer. A second MaxPooling1D layer with a pool size of 4 continues the downsampling process.
   (v) LinformerSelfAttention layer. The LinformerSelfAttention mechanism with a projection dimension $k = 256$ is applied to efficiently capture long-range dependencies within the coarse-scale features.

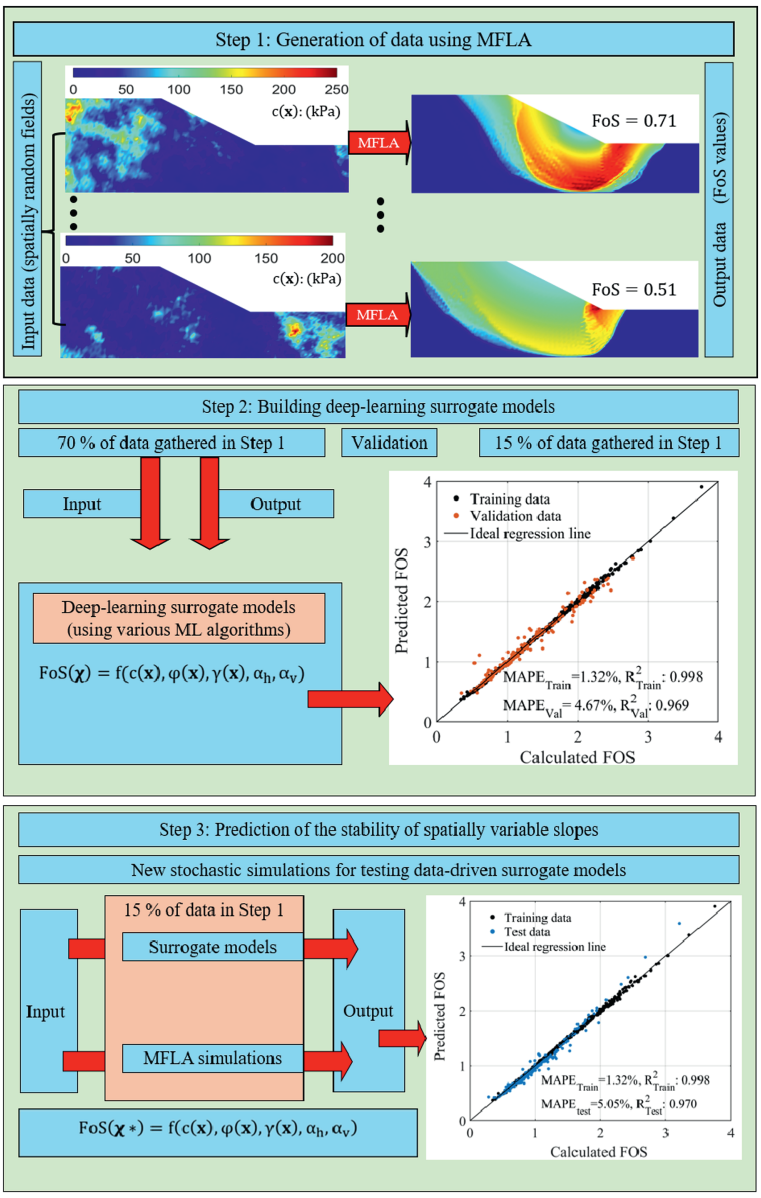

Fig. 10. Illustration of building a multi-downsampling hybrid Linformer-CNN model for the undrained stability of spatially variable slopes.

Each pathway processes the input sequences at different scales, enabling the model to capture both fine and broad patterns within the data.

2.3.3. *Feature fusion and global modeling*

The outputs from the two parallel pathways are concatenated to form a unified feature representation.

2.3.4. *Prediction and model optimization*

Finally, the fused and globally modeled features are fed into an FCN, which outputs the predicted FOS for slope stability. During training, the model continuously adjusts its parameters through backpropagation to minimize prediction errors. The generalization capability of the model is validated using separate validation and testing datasets to ensure robustness and reliability.

Compared to traditional single-architecture models, the proposed hybrid model more effectively leverages the inherent characteristics of irregular slope geometries and random field inputs by integrating both local and global perspectives. In terms of simulation cost, the DL model offers a significant advantage over cumbersome numerical simulations by providing rapid prediction results once training is complete. This efficiency makes the model a highly effective and reliable tool for slope stability analysis.

3. Validation of numerical analysis

Firstly, the MFLA using NS-FEM is applied to compute the slope stability for a range of slope angles in homogeneous soil with $\varphi = 20^{\circ}$ to prove its robustness in calculating the slope stability. Together with the MFLA, other procedures of the kinematic limit analysis using cell-based smoothed FEM (CS-FEM) and SOCP (Nguyen, 2021b; Nguyen and Nguyen-Son, 2022; Nguyen and Vo-Minh, 2022a) are used to compute seismic slope stability. As shown in Fig. 11, the input properties, including finite element meshes, boundary conditions, material properties, and seismic accelerations, are specified for both static and seismic slope

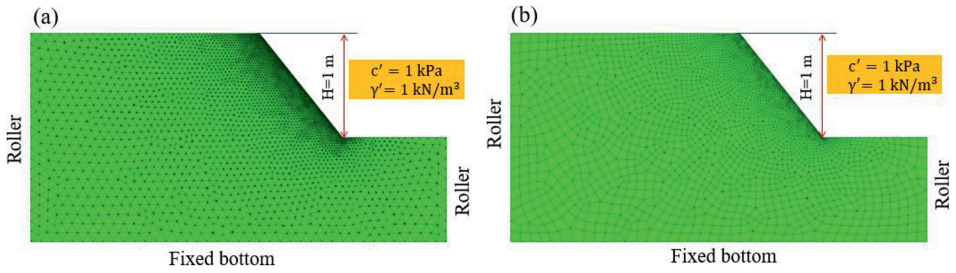

Fig. 11. Meshes and boundary conditions for slope stability under seismic conditions: (a) Triangle and (b) quadratic element meshes.

Table 1
UB and LB for the stability of slopes with various slope angles and $\varphi = 20^{\circ}$ ($N_s = \gamma' H / c'$).

Slope angle (°)	N_s value				
	LB (Lyamin and Sloan, 2002a)	UB (Chen and Liu, 1990)	UB (Lyamin and Sloan, 2002b)	UB (Krabbenhøft et al., 2005)	MFLA using NS-FEM
90	5.41	5.50	5.67	5.67	5.48
80	6.58	6.75	6.89	6.89	6.72
70	8.12	8.30	8.44	8.44	8.26
60	10.21	10.39	10.54	10.54	10.33
50	13.44	13.63	13.79	13.79	13.55

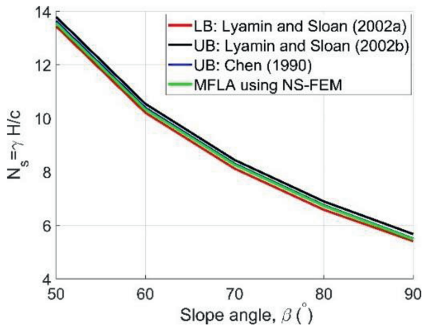

Fig. 12. Slope stability for a range of slope angles in a homogeneous soil with $\varphi = 20^{\circ}$.

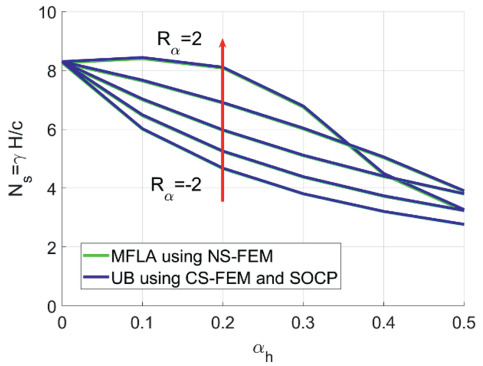

Fig. 13. Comparison of variations of seismic slope stability with $R_\alpha = \alpha_h / \alpha_v$.

stability analyses. The so-called stability number, $N_s = \gamma' H / c'$, serves as a quantity that quantifies the slope stability. To obtain N_s, the choice of $\gamma' = 1, H = 1$, and $c' = 1$ is made in simulations. The numerical results are listed in Table 1, where excellent agreement is found between the novel method and prior contributions. Notably, the present results outperform the classical UB solutions given by Lyamin and Sloan (2002a) and Krabbenhøft et al. (2005). Moreover, the present numerical scheme yields a better slope stability number than Chen and Liu (1990)'s analytical upper bound solution. Fig. 12 illustrates that the present results lie between the lower-bound (LB) solution given by Lyamin and Sloan (2002a) and the UB provided by Chen and Liu (1990), proving the accuracy of the newly proposed numerical approach.

Secondly, a comparison of variations in seismic stability with different combinations of α_h and α_v for a slope with $\beta = 70^{\circ}$ and $\varphi = 20^{\circ}$ is presented in Table 2, revealing excellent agreement between the present results and those obtained by the UB limit analysis using the CS-FEM (Nguyen, 2021b; Nguyen and Nguyen-Son, 2022; Nguyen and Vo-Minh, 2022a). Fig. 13 illustrates that the seismic slope stability results obtained using the proposed method are superior to those provided by the UB using CS-FEM, demonstrating the capabilities of the newly proposed method for calculating seismic slope stability. Moreover, several simulations are carried out to investigate seismic slope stability for various slope angles. As shown in Fig. 13, an upward vertical

Table 2
A comparison of seismic stability numbers for slope with $\beta = 70^{\circ}$ and $\varphi = 20^{\circ}$ ($R_\alpha = \alpha_h / \alpha_v$).

α_h	MFLA using NS-FEM					UB using CS-FEM				
	$R_\alpha = 2$	$R_\alpha = 1$	$R_\alpha = 0$	$R_\alpha = -1$	$R_\alpha = -2$	$R_\alpha = 2$	$R_\alpha = 1$	$R_\alpha = 0$	$R_\alpha = -1$	$R_\alpha = -2$
0	8.26	8.26	8.26	8.26	8.26	8.3	8.3	8.3	8.3	8.3
0.1	8.4	7.64	7	6.46	6	8.44	7.67	7.03	6.49	6.02
0.2	8.08	6.89	5.96	5.24	4.66	8.11	6.91	5.98	5.26	4.68
0.3	6.75	6.01	5.1	4.37	3.8	6.79	6.04	5.12	4.39	3.81
0.4	4.46	5.03	4.39	3.72	3.2	4.5	5.06	4.41	3.74	3.21
0.5	3.22	3.89	3.8	3.23	2.76	3.27	3.91	3.81	3.24	2.77

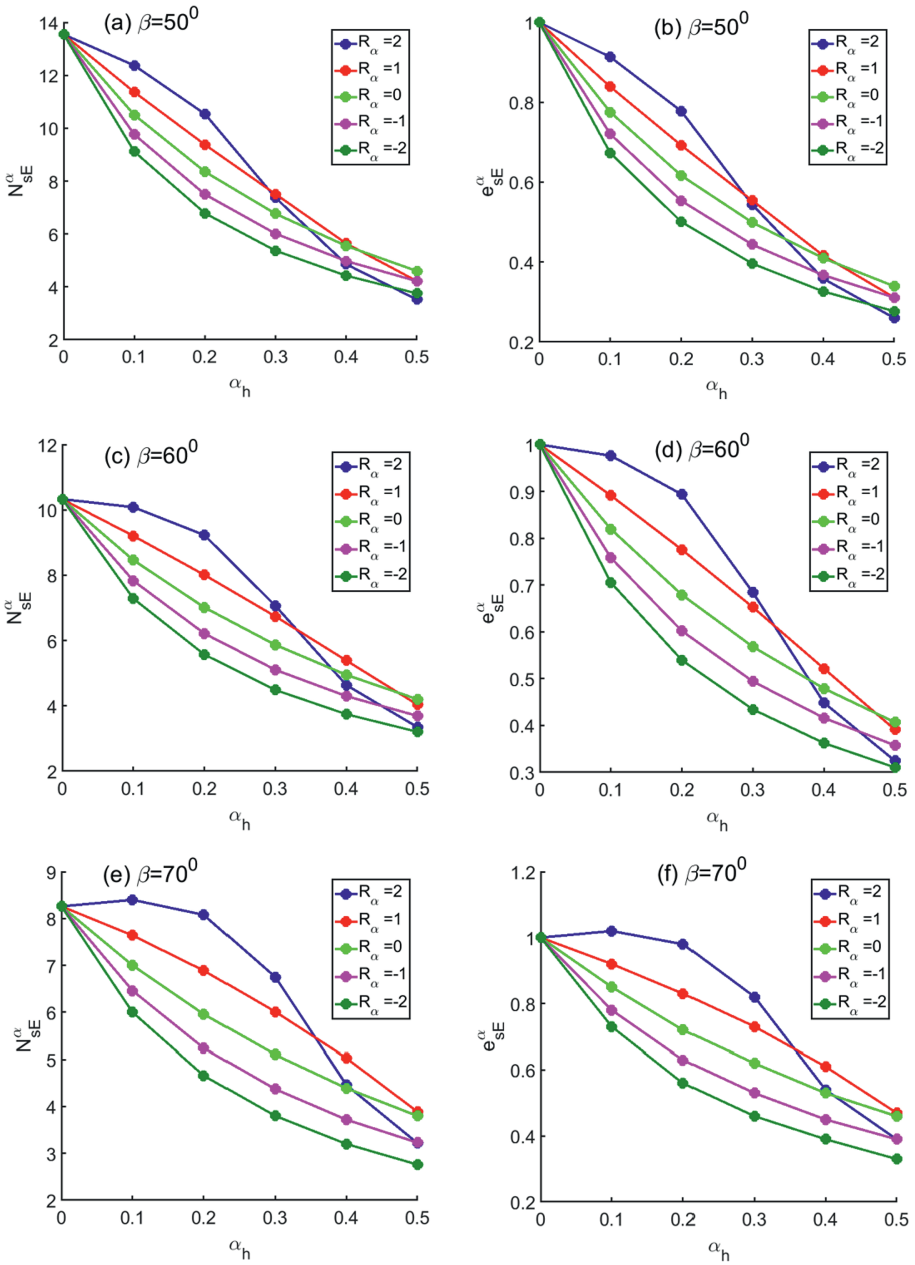

Fig. 14. Variations of the seismic slope stability number and the corrective factor with various ratios ($R_\alpha = \alpha_h/\alpha_v$) for three slope angles with $\varphi = 20^\circ$: (a) N^α_{sE} at $\beta = 50^\circ$; (b) $e^\alpha_{sE} = N^\alpha_{sE}/N_s$ at $\beta = 50^\circ$; (c) N^α_{sE} at $\beta = 60^\circ$; (d) $e^\alpha_{sE} = N^\alpha_{sE}/N_s$ at $\beta = 60^\circ$; (e) N^α_{sE} at $\beta = 70^\circ$; and (f) $e^\alpha_{sE} = N^\alpha_{sE}/N_s$ aat $\beta = 70^\circ$.

Table 3
Characterisation of geotechnical variability for undrained stability analyses using MFLA (Griffiths and Fenton, 2004).

Parameter	μ	ν	l_x	l_y
c_u (kPa)	50	0.8	20	20
φ (°)	0	0	–	–
γ (kN/m^3)	20	0	–	–

seismic acceleration results in a slight increase in the seismic stability number. However, the stability number decreases significantly for positive vertical seismic acceleration at high values of $R_\alpha = \alpha_h/\alpha_v$ (i.e. $\alpha_h \geq 0.3$). The corrective parameter (i.e. $e^\alpha_{sE} = N^\alpha_{sE}/N_s$) representing the reduction in seismic slope stability compared to its static counterpart, is also computed and shown in Fig. 14,

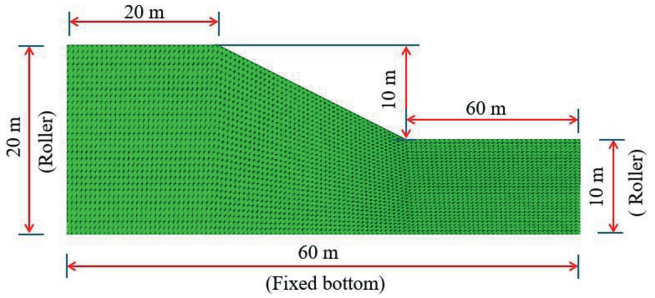

Fig. 15. Meshes, boundary conditions, and geometry of slopes for the undrained stability analyses of spatially variable slopes.

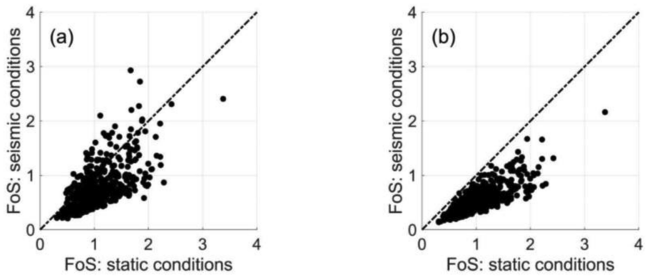

Fig. 16. Comparison between static and seismic slope stability: (a) Upward vertical seismic accelerations; and (b) Downward vertical seismic accelerations.

where a negative vertical seismic acceleration results in a significant drop in seismic stability. It is observed that e^{α}_{sE} almost converges when the value of α_h reaches 0.5, regardless of the value of α_v.

Readers can refer to Nguyen et al. (2025a, b) for more details on the computational efficiency of the numerical framework. Specifically, the reported CPU times reflect the duration spent on the interior-point iterations used to solve stability problems. The analyses included the number of variables, CPU times, and stability numbers for methods employing triangular elements, such as the FEM and edge-based smoothed FEM (ES-FEM) (Nguyen, 2020). These results demonstrate that the current numerical method exceeds the capabilities of smoothed finite element limit analysis, highlighting the effectiveness of our approach in geotechnical engineering analysis.

4. Numerical analysis and DL surrogate models for the stability of spatially variable slopes

This section highlights five key instances to demonstrate the effectiveness of data-driven surrogate models in replacing stochastic simulations for slope stability, particularly in spatial random fields. The potential time and resource savings are significant and impressive. Firstly, we analyze slope stability in a single layer where cohesion and friction angles vary spatially. A series of stochastic simulations using the MFLA is conducted to determine the

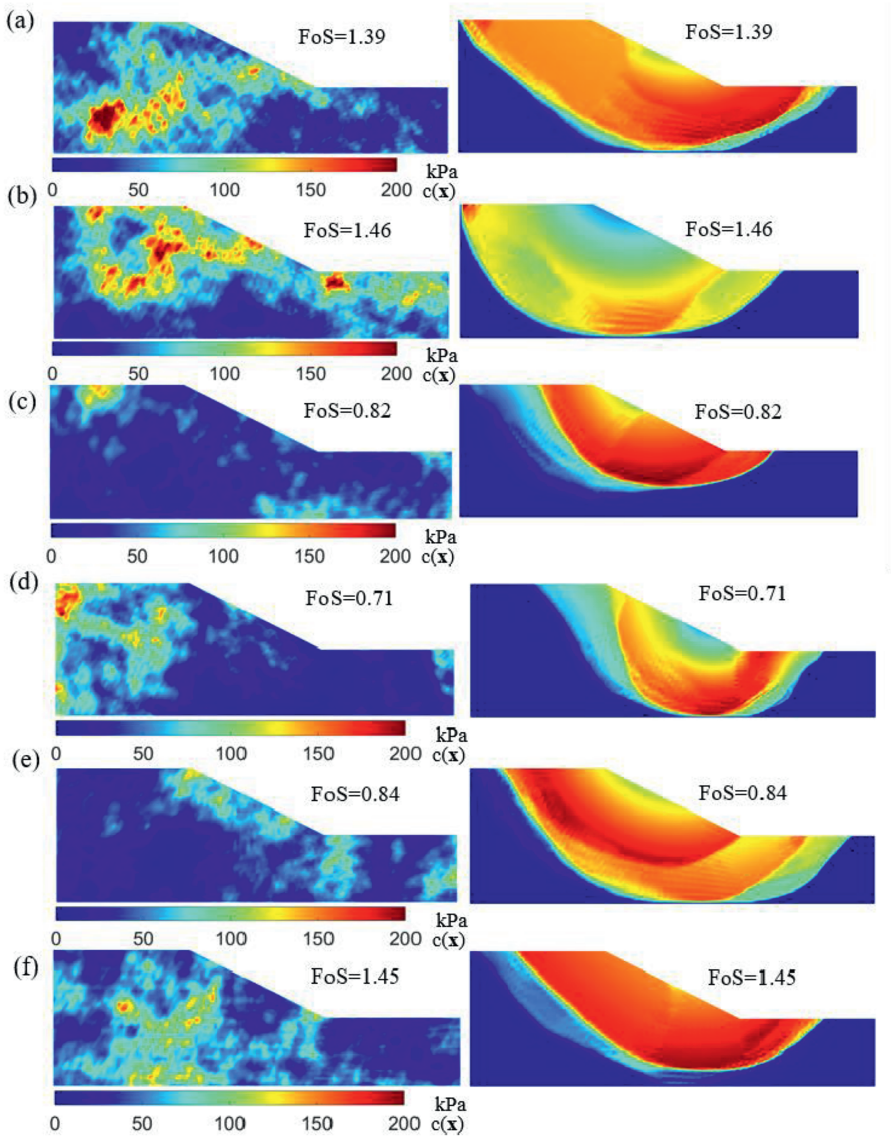

Fig. 17. Correlation of cohesion distributions to failure mechanisms.

undrained stability and the drained stability of the slope. Secondly, we perform stochastic simulations to assess the stability of stratified clay layers, which consist of two layers of clay with spatially random soil properties, also utilizing MFLA. Thirdly, this section investigates the stability of an embankment dam situated on a clay layer. Finally, post-failure slope stability analyses under large deformation are investigated using the newly developed numerical scheme based on the NS-FEM. A brief overview of the process for generating spatially random fields is presented, as this is a crucial step in establishing the statistical parameters needed for MFLA simulations. This process is crucial for conducting stochastic simulations of slope stability, which generate a dataset of FoS values. These values are subsequently employed to develop DL surrogate models, a primary focus of this research, which aims to replace stochastic simulations and thereby reduce computational efforts. The robustness of these data-driven surrogate models is significantly influenced by the choice of ML algorithms. The importance of these algorithms cannot be overstated, as they are the backbone of our intelligent surrogate models. To this end, various DL algorithms are utilized to build these models.

4.1. Undrained stability of spatially variable slopes

Table 3 shows the typical statistical information of soil parameters (Phoon and Kulhawy, 1999; He et al., 2020), where μ and ν are the mean and standard deviation of a log-normal random field, respectively; and l_i denotes the spatial correlation distance in the i direction. Many slope samples with spatial random fields are prepared for stochastic simulations using MFLA (Nguyen, 2023; Nguyen et al., 2025a).

Table 4
Parameters used in CNNs and FCNs algorithms.

Parameter	Value
Neuron	100
Learning rate	0.001
Epoch	5000
Root mean square error (RMSE)	1×10^{-6}

Table 5
Near-optimal hyperparameters used in CNNs and FCNs algorithms.

FCN	CNN
Hidden layer = 2	Hidden layer = 1
$N_{F1} = 600$	$C_1 = 8; C_2 = 16; C_3 = 32$
$N_{F2} = 300$	$N_{F1} = 100$
$L_r = 0.001$	$L_r = 0.001$

Fig. 15 illustrates the meshes, boundary conditions, and computational domains used for undrained stability analyses of spatially variable slopes, specifically corresponding to Example 1 described in He et al. (2020). For all stochastic simulations, the soil weight is set at $\gamma = 20$ kN/m^3, and the friction angle is assumed to be $\varphi = 0°$. The FoS is thus dependent on the spatial variability of the undrained cohesion, represented mathematically as $FoS(\chi) = f(c_u(\boldsymbol{x}))$.

A comparison between the static and seismic FoS values is shown in Fig. 16, where, for all cases, seismic FoS values are smaller than their static counterparts for the downward vertical seismic acceleration. Moreover, the failure pattern and the corresponding FoS value are shown in Fig. 17, where there are no simple links between the magnitude of the FoS value and the failure domain. In addition, Fig. 17 provides insight into the crucial role of undrained cohesion distribution in affecting its FoS value. In particular, the FoS value increases when failure zones have a high undrained cohesion.

Tables 4 and 5 list hyperparameters used to build surrogate models using CNNs and FCNs. Fig. 18 depicts the performance of DL surrogate models to predict FoS values of undrained and drained slope stability, respectively. It is demonstrated that DL surrogate models, utilizing CNNs and FCNs, effectively handle multiple uncertainties and efficiently predict the values of the FoS. Specifically, Fig. 18a shows the results from a one-dimensional CNN (CNN1D) in static conditions. The black solid lines are ideal regression lines, and the dots represent training data (black dots), validation data (red dots), and testing data (blue dots). All points should fall on the ideal regression line if the data can be perfectly regressed. The mean absolute percentage error (MAPE) directly expresses the difference between the predicted and numerical values from MFLA. In this study, the MAPE values for the training, validation, and testing datasets are 4.8 %, 8.6 %, and 7.2 %, respectively. To avoid overfitting, a large ratio (0.5) of dropout is used. Considering the scale issue between input and output data, a min-max normalization scheme is adopted in this study (i.e. $value_{\text{scaled}} = (value - value_{\min})/(value_{\max} - value_{\min})$. In seismic situations, the regression performance of FCN is not good because the normalized strength matrix and seismic acceleration have no numerical difference. The strength matrices of over 3000 elements in the fully connected layer input can quickly dilute the weight of the two seismic accelerations. Therefore, CNN was adopted in this study under different conditions.

Fig. 19 compares the calculated and predicted FoS using various ML methods (i.e. FCNs, CNNs, and LCNs). The surrogate models using FCNs fail to accurately predict the FoS with a low correlation coefficient (R^2) of 0.558 for the testing set. Both CNNs and LCNs produce more accurate predictions for the testing set with a high

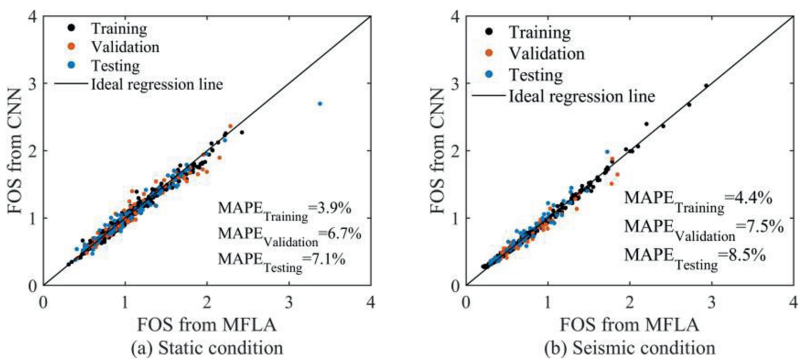

Fig. 18. DL surrogate models for predicting FoS values for Example A.

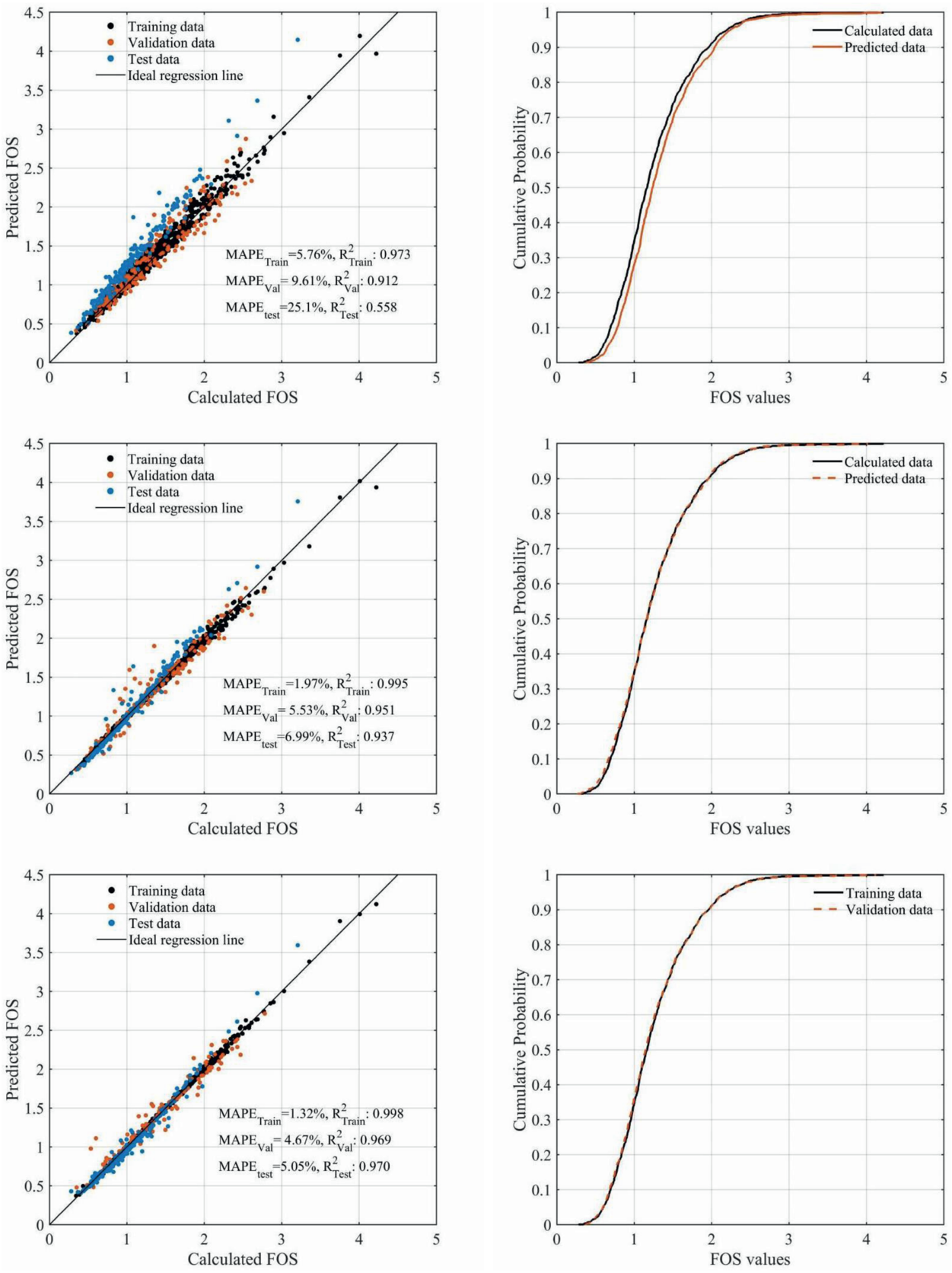

Fig. 19. DL surrogate models employing various ML algorithms to predict the FoS value and the cumulative probability of the FoS for spatially variable slopes with $\gamma = 16$ kN/ m^3: (a) Predicted FoS values using FCNs; (b) Cumulative probability of predicted FoS value using FCNs; (c) Predicted FoS values using CNNs; (d) Cumulative probability of predicted FoS value using CNNs; (e) Predicted FoS values using LCNs; and (f) Cumulative probability of predicted FoS value using LCNs.

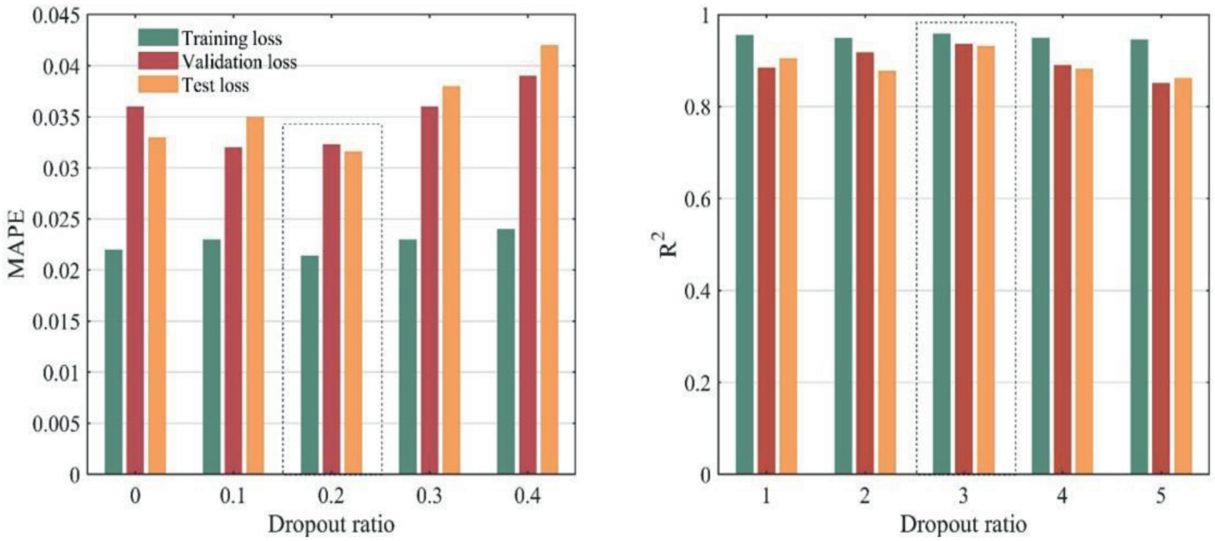

Fig. 20. MAPE and R^2 for different dropout ratios.

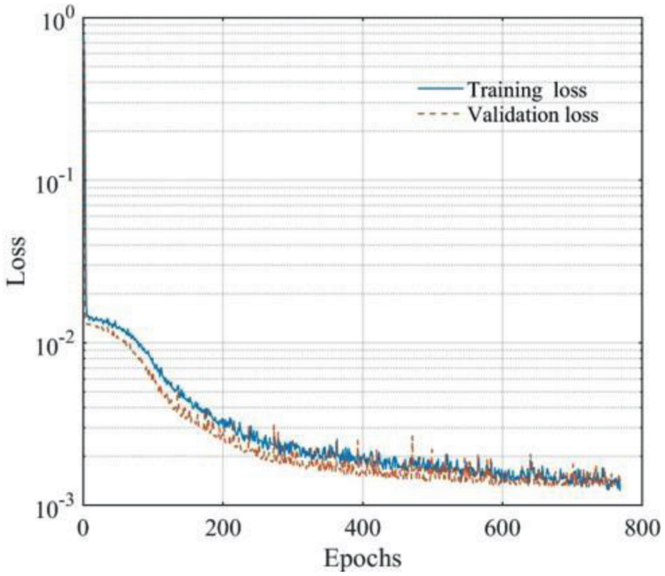

Fig. 21. Training loss for surrogate models shown in Fig. 19.

Table 6
Characterisation of geotechnical variability for drained stability analyses using MFLA (He et al., 2020).

Parameters	μ	ν	l_x	l_y
c_u (kPa)	50	0.8	20	20
φ (°)	20	0.2	10	10
γ (kN/m^3)	20	0	–	–

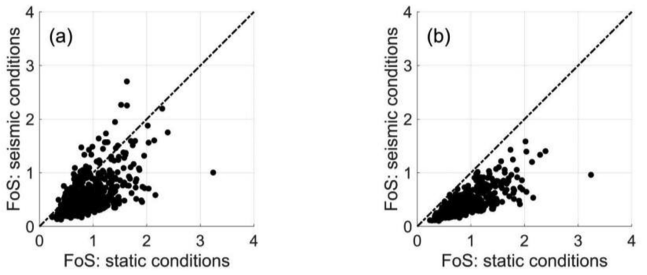

Fig. 23. Comparison between static and seismic slope stability: (a) upward vertical seismic accelerations; and (b) downward vertical seismic accelerations.

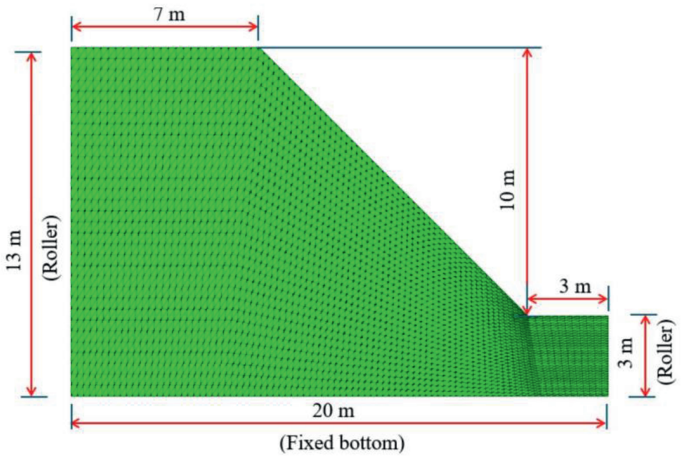

Fig. 22. Meshes, boundary conditions, and geometry of slopes for drained stability analyses of spatially variable slopes.

R^2 of 0.937 and 0.97, respectively. The cumulative probability of FoS for the validating data aligns well with the training data in both CNNs and LCNs. However, it deviates from the training set in FCNs. This further emphasizes the advantages of CNNs and LCNs over FCNS for the FoS predictions of spatially variable soil slopes.

It took several minutes to complete a simulation, requiring several hours to several days to gather data for thousands of stochastic simulations using the current numerical approach. Interestingly, the DL surrogate model significantly reduces computational efforts and time required to obtain such a large amount of data with quite accurate levels. For instance, it took up to 4 h to display all FoS data in Fig. 19; however, we can predict such an amount of FoS data in less than 5 min. It is worth noting that DL surrogate models can replace the stochastic simulations, where predicted and calculated FoS values are almost equal.

Dropout is a regularization technique that helps to prevent overfitting by randomly deactivating a portion of the neurons during training. An excessively high dropout rate could hinder the model's ability to learn, while a too low rate may not offer adequate regularization, leading to overfitting. Following preliminary experiments, a rate of 0.2 is used, which effectively regularizes the model without sacrificing much learning capacity. Specifically, this value enables the model to learn efficiently without becoming overly reliant on specific features, which can

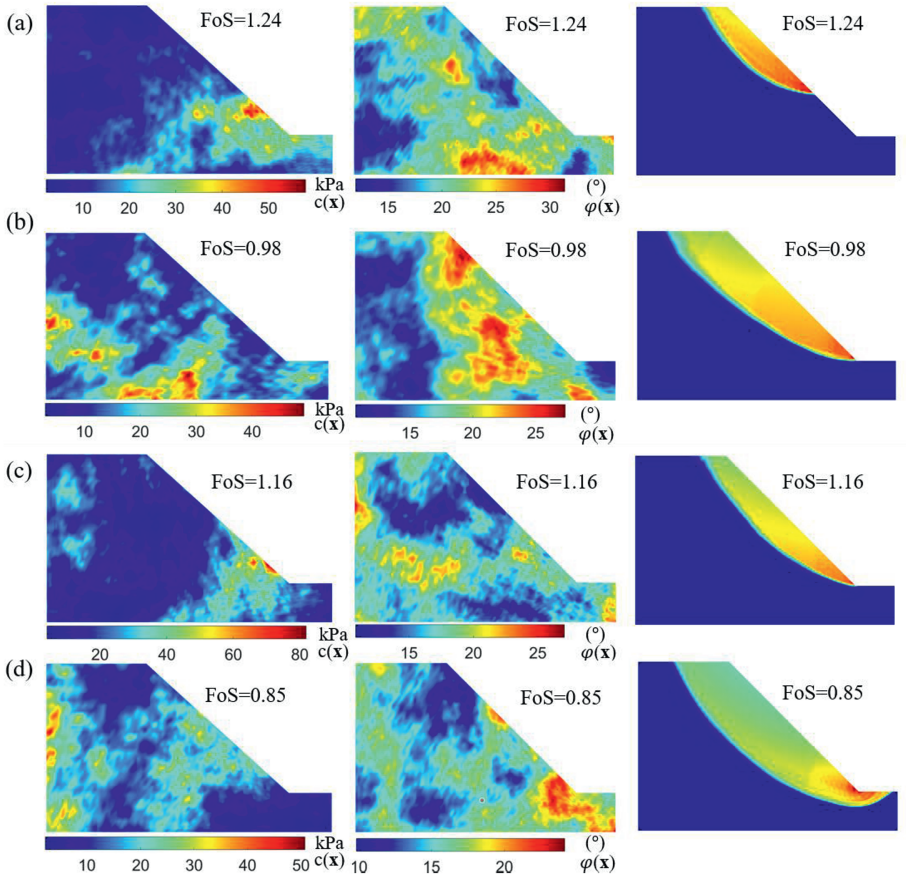

Fig. 24. Effects of spatial variables on failure patterns and corresponding FoS values.

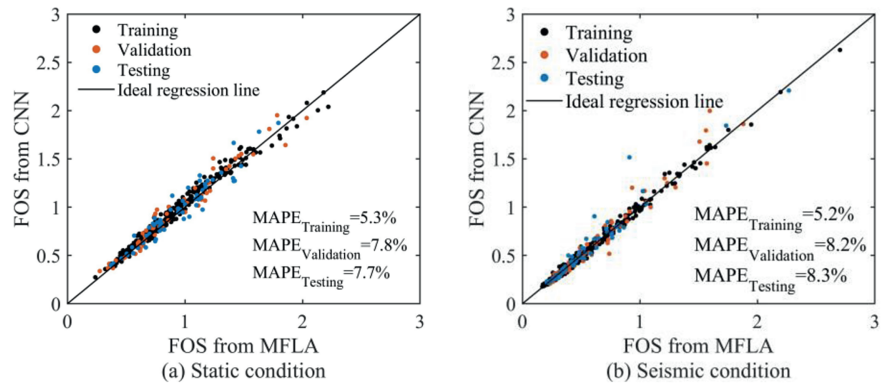

Fig. 25. DL surrogate models for predicting FoS values: (a) Static conditions; and (b) Seismic conditions.

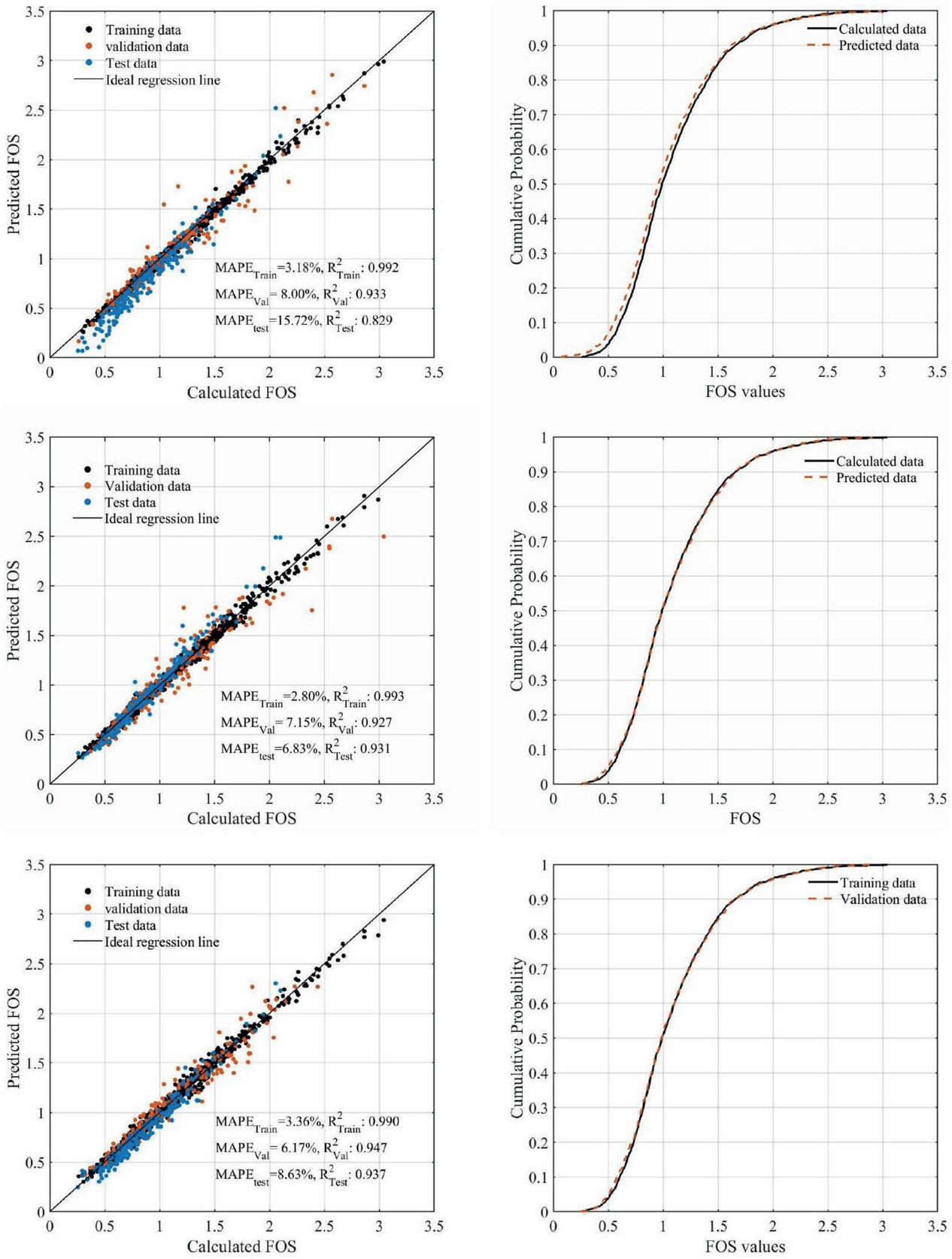

Fig. 26. DL surrogate models using various ML algorithms for predicting the FoS value and the cumulative probability of FoS value of the slope with $\gamma = 16$ kN/ m^3: (a) Predicted FoS values using FCNs; (b) Cumulative probability of predicted FoS value using FCNs; (c) Predicted FoS values using CNNs; (d) Cumulative probability of predicted FoS value using CNNs; (e) Predicted FoS values using LCNs; and (f) Cumulative probability of predicted FoS value using LCNs.

potentially cause overfitting, particularly in small or noisy datasets. The results demonstrate the model's performance under various dropout ratios. There is no significant difference between the various dropout rates; however, a rate of 0.2 has a slightly better effect (see Fig. 20).

A learning rate of 0.0001 was chosen after initial experiments to select a value that guarantees stable convergence of the model. Fig. 21 shows a plot of the training loss, with blue and red lines representing the training and validation loss, respectively. The figure demonstrates that the model has reached reasonable convergence. When training complex architectures such as CNNs and FCNs, a lower learning rate, like 0.0001, is often preferred to ensure optimization stability and gradual convergence. An excessively high learning rate could cause unstable training or poor convergence, while an excessively low learning rate might lead to longer training times or getting stuck in suboptimal solutions.

4.2. Drained stability of spatially variable slopes

Fig. 22 illustrates the typical mesh configurations, boundary conditions, and geometry of slopes employed in drained stability analyses. All statistical parameters of the spatially random field are detailed in Table 6. Notably, the spatial distribution of cohesion, $c(\boldsymbol{x})$, closely resembles the undrained stability example described earlier, as outlined in Table 3. The mean value $\mu_{\varphi} = 20°$ and the standard deviation $\nu_{\varphi} = 0.2$ for the spatially log-normal distribution of the friction angle ϕ ($\boldsymbol{x}$) are specified, with a spatial correlation distance of $l_{\varphi} = 10$. The boundary conditions and computational domains are consistent with those presented in Example 2 by He et al. (2020). The soil weight is set for all stochastic simulations to $\gamma = 20$ kN/m^3.

A comparison between the static and seismic FoS values is shown in Fig. 23, where, for all cases, seismic FoS values are smaller than their static counterparts for the downward vertical seismic acceleration. Moreover, Fig. 24 links the failure pattern to the distribution of spatial friction angle. FoS values increase when a high magnitude of friction angle is distributed into failure zones.

Fig. 25 exhibits the performance of DL surrogate models to predict FoS values of undrained and drained slope stability, respectively. It is shown that DL surrogate models using CNNs and FCNs effectively handle multiple uncertainties and efficiently predict the FoS values. Fig. 25 illustrates the prediction performance of DL-based surrogate models for FoS under static and seismic conditions, where both cohesion and friction angle are considered as input random fields. Compared with Fig. 18, with cohesion as the only spatially variable parameter, Fig. 25 represents a more complex input configuration with increased channel dimensionality. The CNN-based surrogate model maintains stable and accurate regression performance under both loading conditions. The predicted FoS values remain closely distributed around the ideal regression line for the training, validation, and testing datasets. The magnitude of the mean absolute percentage error (MAPE) remains consistent with that observed in Example A, indicating that the CNN architecture is robust to variations in both the number and type of geotechnical input parameters. In

Table 7
Statistical properties of soil parameters for a two-layered hypothetical slope (Ching et al., 2009).

Clay layer	Parameter	μ	ν	l_x	l_y
1	c_u	120 kPa	0.3	10	10
	φ	0°	0	–	–
	γ	19 kN/m^3	0	–	–
2	c_u	160 kPa	0.3	10	10
	φ	0°	0.0	–	–
	γ	19 kN/m^3	0	–	–

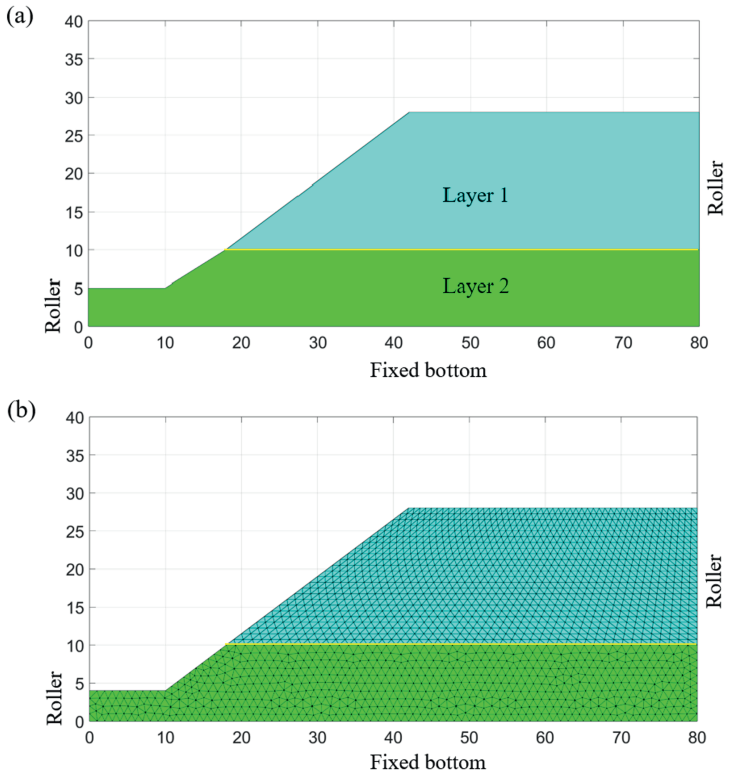

Fig. 27. Meshes and boundary conditions of two-layered slopes in spatially random soils: (a) Layered slope geometry; and (b) Meshes and boundary conditions.

particular, the testing MAPE values for slopes in Example B are approximately 7 %–8 % under static conditions and around 8 %–9 % under seismic conditions, which are comparable to the results obtained in Fig. 18. This consistency demonstrates that the CNN-based surrogate model can effectively capture global spatial correlations in slope stability problems, even when multiple random fields are simultaneously considered. The uniform mesh and consistent spatial adjacency adopted in the MFLA framework further facilitate the application of CNNs to different problem configurations without requiring structural modifications to the network architecture.

Fig. 26 shows the calculated and predicted FOS of drained slopes in spatially variable cohesive and frictional soils, based on calculated and predicted FoS. The results indicate the same trend: FCNs produce the worst predictions of FoS, while LCNs achieve the best predictions. However, compared to the predicted FoS of the undrained slopes with spatially variable cohesion in Fig. 19, the DL surrogate model produces a lower resolution for the predicted FoS of the drained slopes in Fig. 26. This can be attributed to the bivariable cohesion and friction random fields for the drained slopes, which introduce additional uncertainties and reduce the prediction accuracy of the FoS.

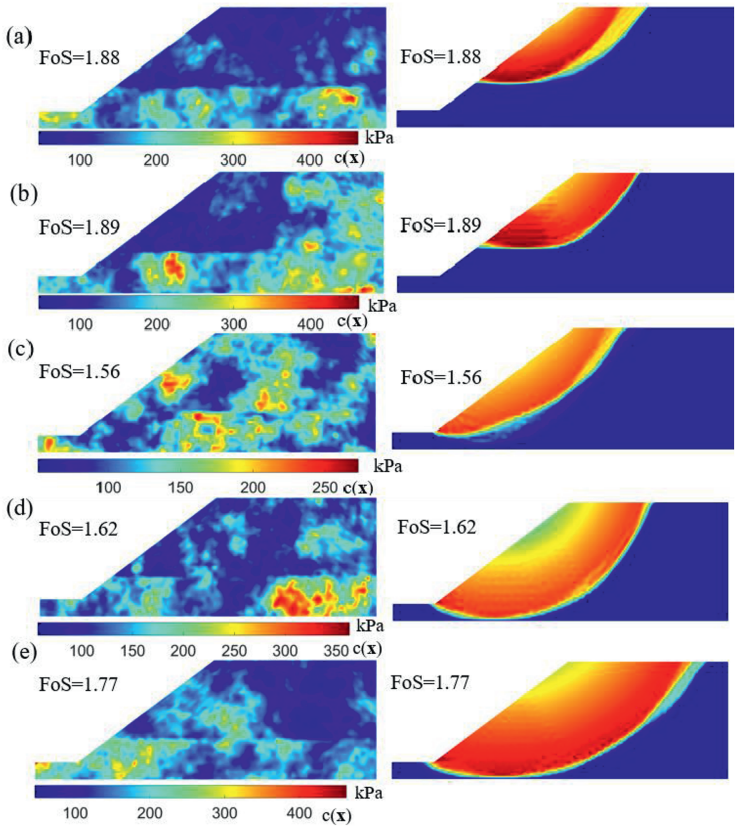

Fig. 28. Effects of spatial cohesion distribution on the failure pattern and the corresponding FoS value of the stratified clayed slope.

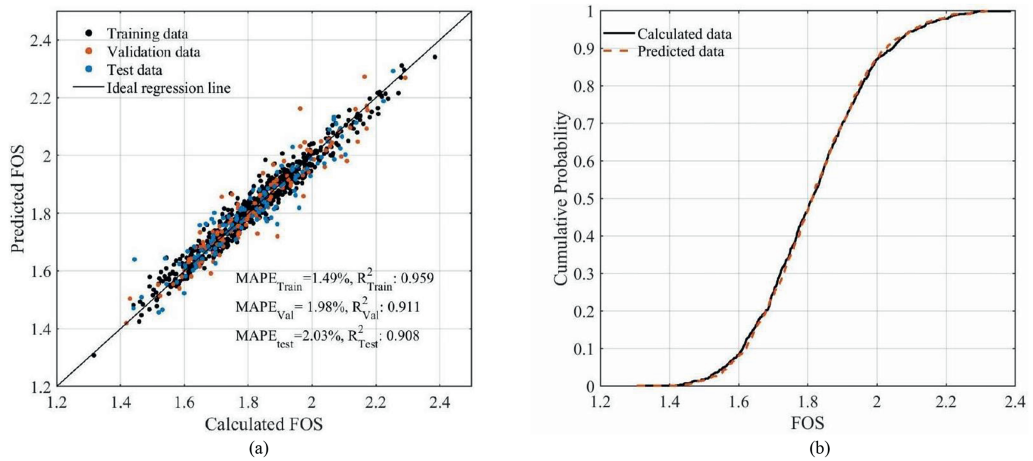

Fig. 29. DL surrogate model using hybrid Linformer-CNNs for predicting the FoS value and the cumulative probability of FoS value for two-layer slopes: (a) Predicted FoS values; and (b) Cumulative probability of predicted FoS value.

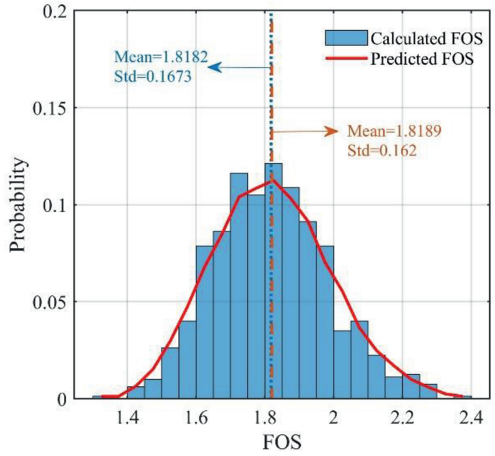

Fig. 30. Frequency distribution of FoS values from DL surrogate models using hybrid Linformer-CNNs.

4.3. Stability analysis of layered slopes with spatially random soils

Following the work of Ching et al. (2009), a series of stochastic simulations was conducted to assess the stability of a stratified slope comprising two clayed layers. The geometry, mesh configurations, and boundary conditions for these two-layered slopes in spatially random soils are illustrated in Fig. 27, where the weaker clay layer is situated atop the stronger one.

In this analysis, uncertainty in the undrained shear strength for both layers is modeled using a lognormal distribution with a coefficient of variation (COV) of 0.3. The statistical properties of the soil parameters for the hypothetical two-layered slope are summarized in Table 7.

According to Ching et al. (2009), two distinct failure modes can occur. The first failure mode arises within the upper layer, influenced by its inherent uncertainties, while the second can propagate through both layers. Fig. 28 illustrates the failure patterns and

Table 8
Statistical properties of soil parameters for an embankment dam resting on a clay layer using MFLA (Chowdhury and Xu, 1995).

Layer	Parameter	μ	ν	l_x	l_y
1	c	10 kPa	0.2	10	10
	φ	12°	0.25	10	10
	γ	20 kN/m^3	0	–	–
2	c_u	40 kPa	0.2	10	10
	φ	0°	0	–	–
	γ	18 kN/m^3	0	–	–

the corresponding FoS for various distributions of undrained shear strength, highlighting the impact of uncertainties in the two clayed layers on the stability of stratified slopes.

Notably, Fig. 28a and b demonstrates that failure predominantly occurs within the upper layer when the weaker clay layer is positioned above the stronger one. Furthermore, the failure zone expands and deepens, manifesting shear bands associated with the weaker undrained shear strength, as depicted in Fig. 28c–e. These observations underscore the importance of conducting stochastic analyses for evaluating slope stability.

A series of computational analyses was conducted to evaluate the FoS values of stratified clay slopes. The numerical results obtained from these analyses were subsequently utilized to train ML algorithms for constructing surrogate models. As illustrated in Fig. 29, the DL surrogate model employing the hybrid Linformer-CNN exhibits a strong capability for accurately predicting FoS values. Notably, the predicted FoS values closely align with the numerical results, as indicated by their proximity to the perfect regression line (Fig. 29a).

Furthermore, the MAPE for validation ($MAPE_{val}$ = 2.23 %) and testing ($MAPE_{test}$ = 2.03 %) provides compelling evidence of the efficacy and reliability of the DL surrogate models in estimating the FoS for stratified slopes. Both numerical and predicted FoS values are used to plot the cumulative probability, as shown in Fig. 29b, demonstrating no discrepancies between these values.

Additionally, we compare the frequency distribution of FoS

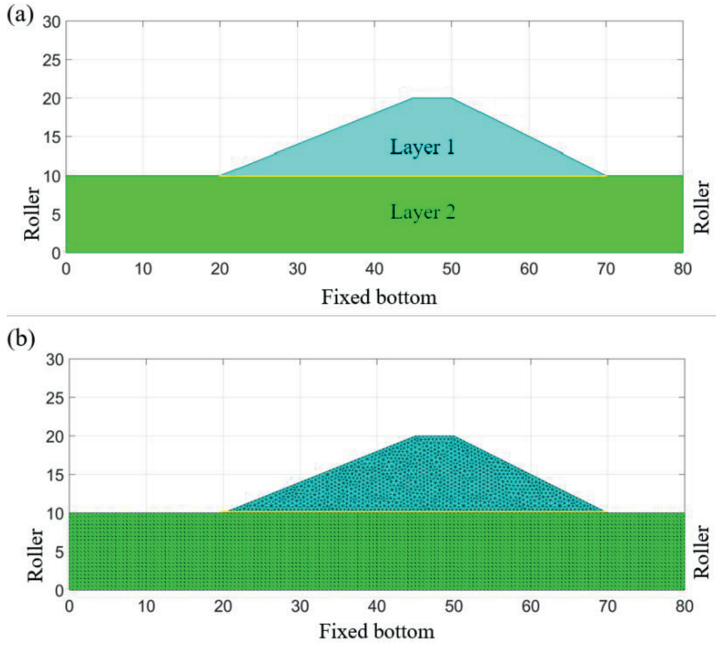

Fig. 31. (a) Geometry and (b) meshes and boundary conditions of an embankment dam with spatially random soils.

values derived from MFLA simulations with those predicted by DL surrogate models utilizing hybrid Linformer-CNNs. As shown in Fig. 30, both approaches yield nearly identical mean FoS values, specifically, $\mu_{FoS} = 1.8181$ for the MFLA simulations and $\mu_{FoS} = 1.8202$ for the predictions from the DL surrogate model. These comparisons validate the capability of DL surrogate models to effectively replace stochastic simulations when assessing the stability of stratified clay slopes.

4.4. *Stability analysis of an embankment* dam with spatially random soils

In addition, we evaluate the stability of a fill embankment supported by a clay layer using the modified FEM (MFLA). Fig. 31 presents the geometry of the embankment dam, along with the corresponding mesh and boundary conditions, incorporating the effects of spatially random soil properties. The sizes of the computational domains and the soil properties used in our analysis are consistent with the examples provided by Chowdhury and Xu (1995). Detailed statistical characteristics of the soil parameters are presented in Table 8, where the clay layer has a unit weight of $\gamma = 18\ \mathrm{kN/m^3}$. The spatially random cohesion is described by a mean value of $\mu_{c_u} = 40$ kPa and a COV of $\nu_{c_u} = 0.2$.

A total of 800 stochastic simulations were conducted to develop surrogate models using various ML algorithms. These models aim to replace the traditional stochastic analysis of the stability of embankment dams supported by spatially variable clay layers. Fig. 32 demonstrates the variation in failure patterns corresponding to different spatial cohesion distributions, highlighting how shear bands tend to form along weak zones in the undrained cohesion. For example, when the embankment dam rests on a relatively strong clay layer, failure is confined to the first layer, as shown in Fig. 32a. However, as the undrained shear strength of the clay layer diminishes, the failure zone deepens, indicating increased vulnerability of the dam, as illustrated in Fig. 32c and d.

The obtained FoS values and their corresponding random fields are used to train ML-based surrogate models. Fig. 33 compares the calculated and predicted FoS values using three different surrogate models: CNNs, LCNs, and hybrid Linformer-CNNs. All three models demonstrate the capability to predict the FoS of an embankment dam with spatially random soils. However, the hybrid Linformer-CNN-based surrogate model delivers the most accurate predictions, achieving the highest correlation coefficients ($R^2 = 0.959$) for the training data and $R^2 = 0.932$ for the testing data. In contrast, the CNN-based surrogate model exhibits the weakest performance, with the lowest R^2 of 0.877 for the training data and 0.631 for the testing data. The cumulative probability comparison of FoS, as shown in Fig. 33, further reinforces these findings. These results indicate that the hybrid Linformer-CNN-based surrogate model offers the highest precision and is the most suitable for predicting the FoS of an embankment dam with spatially random soils.

Fig. 34 presents the distribution of predicted FoS values based on CNN and hybrid Linformer-CNN surrogate models. Both methods effectively estimate the mean FoS. For example, the CNN-based surrogate model predicts a mean FoS of 0.9447, while the hybrid Linformer-CNN-based surrogate model predicts a mean FoS of 0.9505. Both values are very close to the calculated mean FoS of 0.9466. However, when it comes to the standard deviation, the hybrid Linformer-CNN-based surrogate model performs notably better, predicting a standard deviation of 0.1247, which closely matches the calculated value of 0.1311. Conversely, the CNN-based surrogate model predicts a standard deviation of 0.1032, which is significantly lower than the estimated value. This discrepancy could lead to incorrect predictions of the FoS distribution and

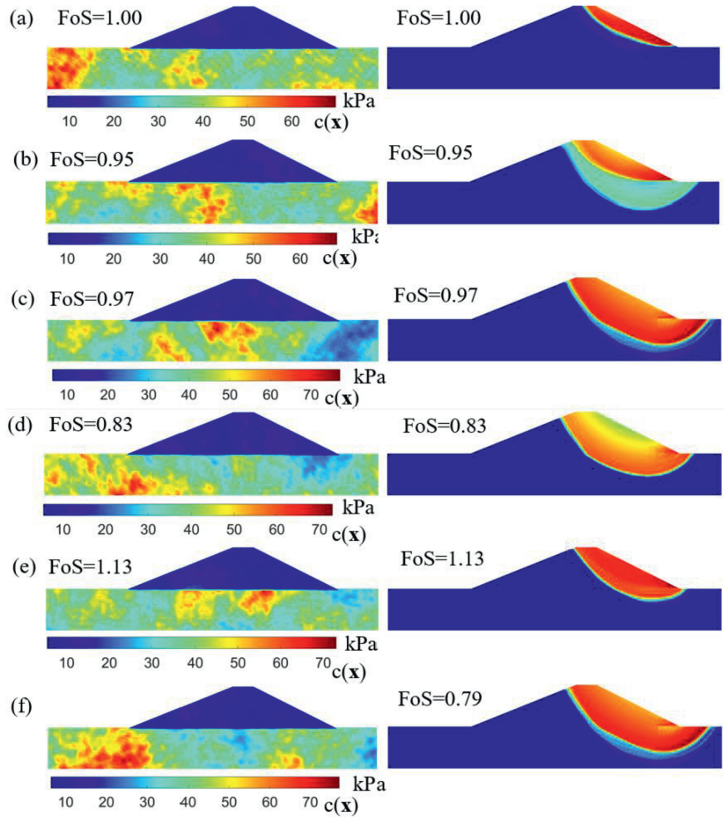

Fig. 32. Effects of spatial cohesion distribution on the failure pattern and the corresponding FoS value of an embankment dam.

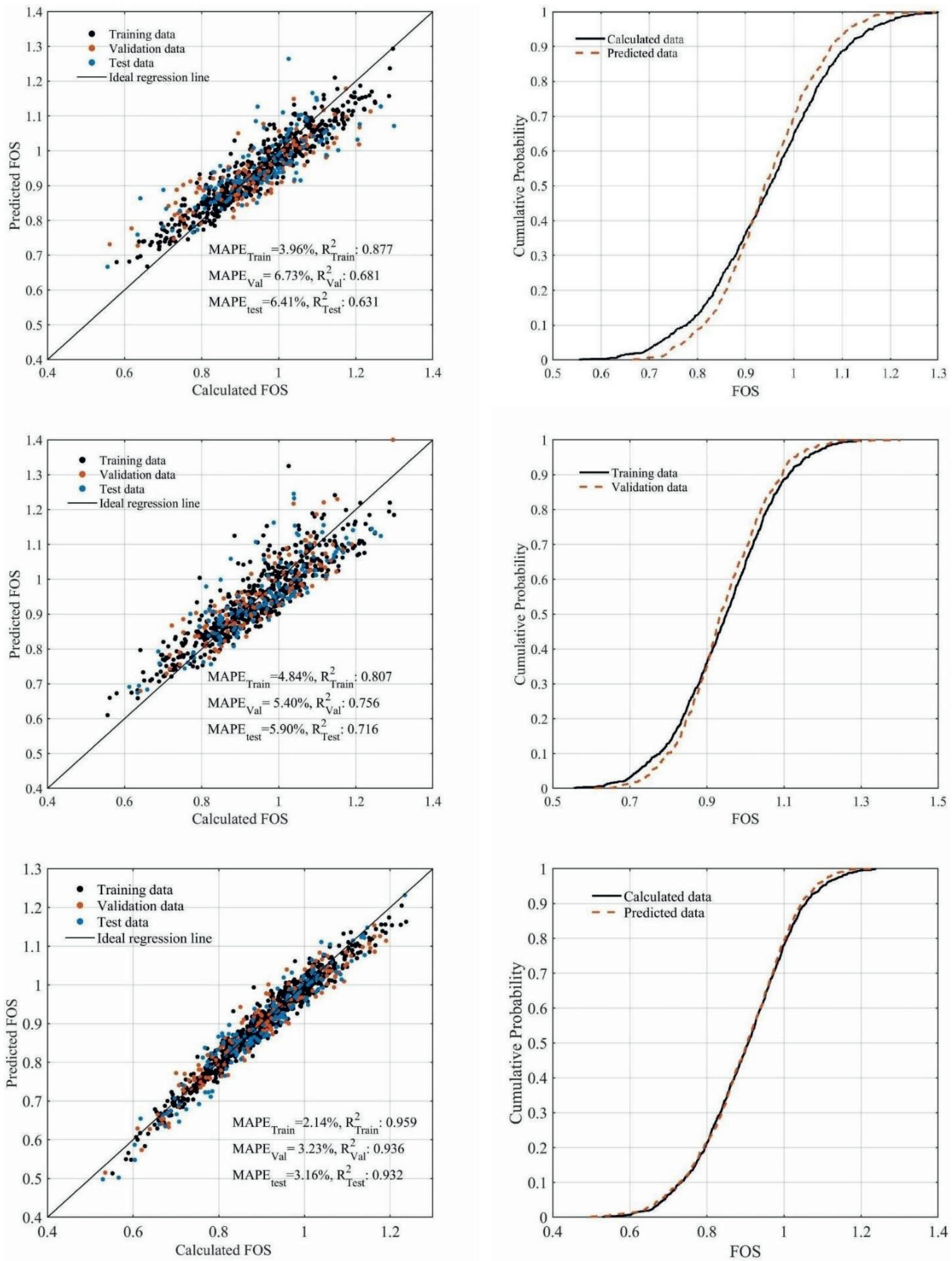

Fig. 33. DL surrogate models using various ML algorithms for predicting the FoS value and the cumulative probability of FoS value for an embankment dam: (a) Predicted FoS values using CNNs; (b) Cumulative probability of predicted FoS value using CNNs; (c) Predicted FoS values using LCNs; (d) Cumulative probability of predicted FoS value using LCNs; (e) Predicted FoS values using hybrid Linformer-CNNs; and (f) Cumulative probability of predicted FoS value using hybrid Linformer-CNNs.

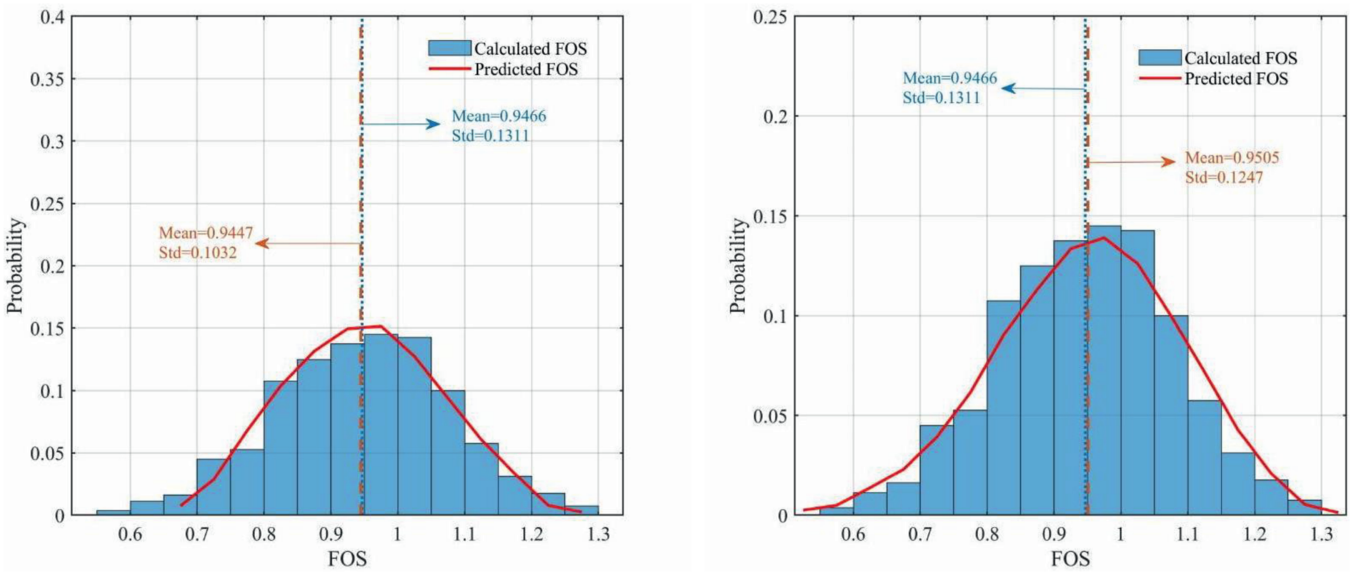

Fig. 34. Frequency distribution of FoS values from DL surrogate models using (a) CNNs and (b) hybrid Linformer-CNNs. Std denotes the standard deviation.

cumulative probability, thereby impacting the reliability assessment and risk estimation of dam failure.

These findings suggest that the hybrid Linformer-CNN-based surrogate model is the superior choice for predicting the FoS and its distribution of an embankment dam with spatially random soils. Moreover, they underscore the importance of selecting the most appropriate ML methods for constructing surrogate models to ensure accurate and reliable predictions for the performance and behavior of spatial variable geo-structures.

4.5. Post-failure analysis using the newly developed sequential limit analysis

We investigate the post-failure of spatially variable slopes using the example of drained stability (see Fig. 22), where the cohesion and friction angle are spatial random fields. Fig. 35 depicts the evolution of a typical post-failure landslide simulated by the newly developed sequential limit analysis based on the Hellinger-Reissner functional using NS-FEM. In Step 1, initial failure is captured using the mixed limit analysis formulation. However, plastic strain bands form and become increasingly pronounced as the simulation progresses, leading to increased instability and a corresponding increase in the FoS value. The landslide exhibits both forward motion and retrogressive slip surfaces, resulting in soil loss and instability in the direction of the landslide flow. Herein, we assessed the failure pattern and its corresponding failure at three different large deformations, and several quasi-rotational slip surfaces are visible, suggesting that a complex failure pattern has developed. These intricate failure bands result from the spatial variability of the random fields, which refers to the non-uniform distribution of cohesion and friction angle across the slope, as well as the horizontal layering, or the stratification of the soil layers in a horizontal direction.

In addition, we monitored the position of the crest (i.e. the point X) and the corresponding FoS values using the newly developed numerical scheme based on nodal smoothing domains, as illustrated in Fig. 36. The capabilities of surrogate models in predicting stability and conducting post-failure analyses of spatially variable slopes are demonstrated in Figs. 35 and 37. Notably, the DL surrogate model excels at predicting FoS values throughout various phases of a typical post-failure landslide, underscoring its practical implications.

Our observations indicate that FoS values tend to increase alongside forward movement and retrogressive slip surfaces, likely due to soil loss and resulting instability. Furthermore, the surrogate model effectively captures the position of the crest during the progression of post-failure landslides, reinforcing the practical relevance of our findings. The predicted values for the crest's position closely align with the calculated values, resulting in a nearly perfect regression line (Fig. 37a and b).

4.6. Model limitations and transferability

The model developed in this study has demonstrated exemplary performance in predicting slope stability within the specific geological contexts represented in the training dataset. However, it is essential to note that the model's performance may be limited when applied to significantly different geological conditions. The primary limitations are as follows.

(1) Limited training data scope

The model was trained using a specific set of slope configurations and soil properties. As such, it may not generalize well with conditions that deviate substantially from those represented in the training dataset. For instance, the model was trained in random fields generated under specific assumptions about the spatial variability of soil parameters. Therefore, extreme geological conditions such as materials with very different characteristics (e.g. rock) might not be adequately predicted by the model.

(2) Sensitivity to input variability

The accuracy of our model is strongly dependent on the representativeness of the input data. It is supposed that the training dataset does not encompass a wide range of soil properties, slope geometries, or boundary conditions. In that case, critical dependencies may be overlooked, potentially leading to inaccurate predictions in contexts not represented in the dataset.

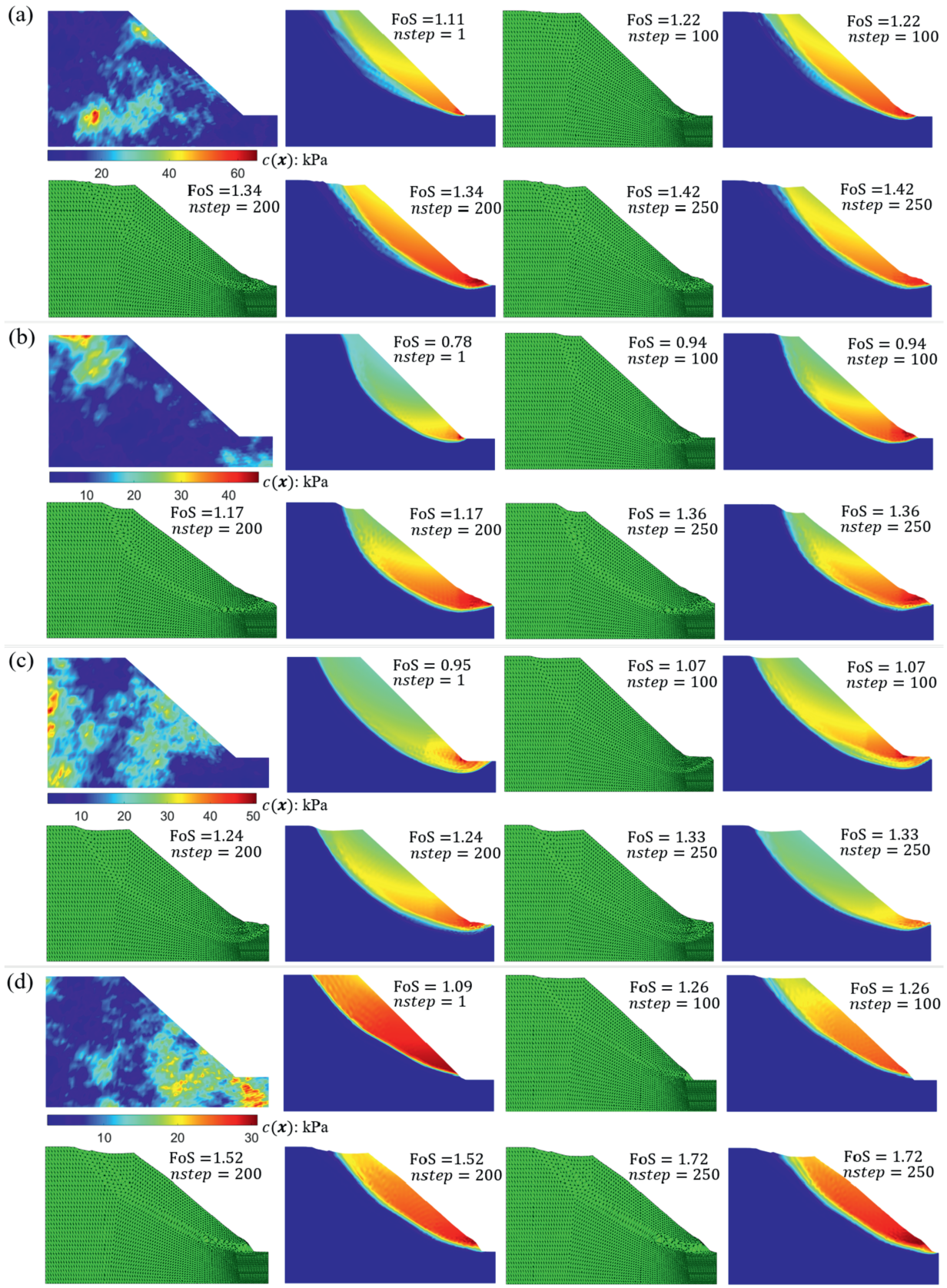

Fig. 35. Effects of spatial cohesion distribution on the failure pattern and the corresponding FoS value for various time steps.

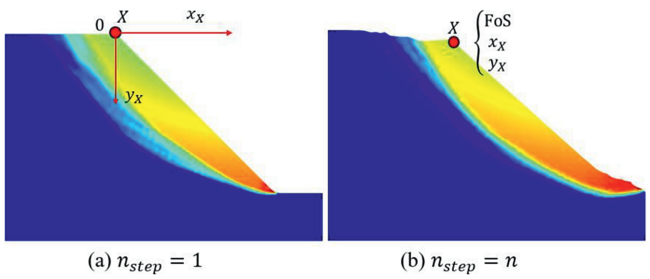

Fig. 36. Illustration of the stability and post-failure analyses using the newly developed SSLA: (a) Initial failure of spatially variable slopes; and (b) Post-failure of spatially variable slopes.

(3) Transferability to unrepresented geological contexts

Although the current model is tailored to specific slope configurations, its DL architecture offers potential for transferability. By retraining or fine-tuning with new data from diverse geological contexts, the model can adapt to novel conditions. Techniques such as transfer learning and domain adaptation may further enhance its generalizability. In future work, we plan to integrate additional external datasets covering diverse geographical regions, soil types, and slope configurations to expand the model's applicability.

5. Conclusions

This study presents a novel framework that integrates a newly developed sequential limit analysis based on the Hellinger-Reissner variational principle with an innovative DL architecture, the multi-downsampling hybrid Linformer-CNN model, to evaluate the stability of spatially variable slopes. The NS-FEM-based MFLA significantly enhances computational accuracy and convergence by smoothing strain fields and mitigating numerical discontinuities inherent in traditional FEM. This advancement not only generates reliable datasets for stochastic simulations under both static and seismic loading conditions but also establishes a robust foundation for subsequent DL surrogate modeling.

The core innovation of this research lies in the development of the multi-downsampling hybrid Linformer-CNN model, which effectively combines multi-scale 1D CNNs with Linformer-based self-attention mechanisms. By employing parallel downsampling pathways utilizing AveragePooling1D and MaxPooling1D layers, the model adeptly captures features at varying granularities – medium-scale features through average pooling and coarse-scale features through max pooling. This multi-scale feature extraction is further enhanced by Linformer self-attention layers, which efficiently capture long-range dependencies within the data while maintaining computational and memory efficiency through low-rank approximations.

Comprehensive validation across multiple scenarios, including single-layer slopes, stratified clay layers, and embankment dams, demonstrates the superior performance of the proposed framework. The NS-FEM-based MFLA consistently outperforms classical UB solutions, showcasing its robustness and accuracy in computing the FoS. Concurrently, the multi-downsampling hybrid Linformer-CNN model exhibits exceptional predictive capability, achieving an MAPE below 10 % across training, validation, and testing datasets. Comparative analyses reveal that this hybrid model surpasses traditional FCNs and standard CNNs in both accuracy and reliability, particularly under seismic conditions where CNNs demonstrate enhanced performance over DNNs.

Moreover, the DL surrogate models offer substantial reductions in computational time, effectively replacing resource-intensive stochastic simulations without compromising prediction accuracy. The integration of multi-scale feature extraction with efficient global dependency modeling ensures that the framework is both scalable and adaptable to complex geotechnical conditions. The application of FCNs to integrate multi-scale features further enhances the model's predictive capabilities, enabling the precise estimation of FoS values essential for slope stability assessments.

By merging advanced numerical methods with state-of-the-art DL techniques, the proposed framework provides a highly effective and reliable tool for rapid slope stability analysis. This integration not only enhances the accuracy and efficiency of stability predictions but also facilitates real-time assessments in engineering projects, thereby supporting informed decision-making and risk management.

Efforts should focus on developing a dynamic elastoplastic framework using the θ-method to enhance its robustness in accurately capturing runout distances. Additionally, excluding elastic deformation from the constitutive model introduces a new SSLA that integrates the time domain into the numerical procedure. This approach enables us to consider strength reduction as deformation increases easily. The new framework can be validated against approaches based on the material point method (MPM) (Ma et al., 2022a, b; 2024; Li et al., 2025). These studies offer probabilistic frameworks for landslide analysis, uncertainty quantification, and runout distance modeling, which are pertinent to the future development of the current numerical framework.

Additionally, future improvements could explore a 2D CNN architecture or a spatial attention mechanism that accounts for the 2D nature of spatial correlations in the data, thereby better preserving direct spatial relationships. Alternatively, positional

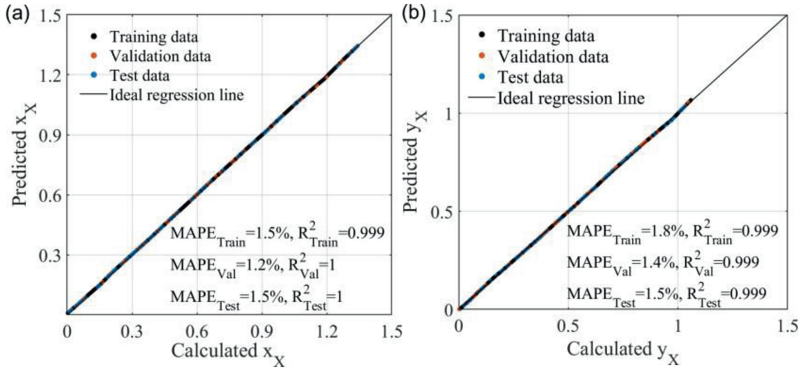

Fig. 37. Calculated and predicted positions of the crest: (a) The movement of the crest in the *x*-direction; and (b) The movement of the crest in the *y*-direction.

encoding or graph-based neural networks may be investigated to represent spatially correlated data more effectively within a DL model.

CRediT authorship contribution statement

H. Xu: Writing – original draft, Methodology, Formal analysis, Conceptualization. **H.C. Nguyen:** Writing – original draft, Validation, Methodology, Formal analysis, Conceptualization. **M. Nazem:** Writing – review & editing, Supervision, Conceptualization. **X. He:** Writing – review & editing, Supervision, Conceptualization. **X. Chen:** Writing – review & editing, Writing – original draft, Conceptualization. **R. Sousa:** Writing – review & editing, Writing – original draft, Supervision, Conceptualization. **J. Kowalski:** Writing – review & editing, Supervision, Conceptualization.

Declaration of competing interest

The authors declare that they have no known competing financial interests or personal relationships that could have appeared to influence the work reported in this paper.

Acknowledgements

The authors express their heartfelt gratitude to anonymous reviewers for their constructive feedback on our research paper. Their insightful comments have significantly enriched the quality of the paper.

References

Abbasi, B., Mahlooji, H., 2012. Improving response surface methodology by using artificial neural network and simulated annealing. Expert Syst. Appl. 39 (3), 3461–3468.
Agbaje, S., Zhang, X., Patelli, E., Ward, D., Dhimitri, L., 2024. Random field failure and post-failure analyses of vertical slopes in soft clays. Comput. Geotech. 166, 106037.
Allaix, D.L., Carbone, V.I., 2011. An improvement of the response surface method. Struct. Saf. 33 (2), 165–172.
Aminpour, M., Alaie, R., Kardani, N., Moridpour, S., Nazem, M., 2023a. Highly efficient reliability analysis of anisotropic heterogeneous slopes: machine learning-aided Monte Carlo method. Acta Geotech. 18 (6), 3367–3389.
Aminpour, M., Alaie, R., Khosravi, S., Kardani, N., Moridpour, S., Nazem, M., 2023b. Slope stability machine learning predictions on spatially variable random fields with and without factor of safety calculations. Comput. Geotech. 153, 105094.
Baghbani, A., Choudhury, T., Costa, S., Reiner, J., 2022. Application of artificial intelligence in geotechnical engineering: a state-of-the-art review. Earth Sci. Rev. 228, 103991.
Bathe, K.J., Wilson, E.L., 1972. Stability and accuracy analysis of direct integration methods. Earthq. Eng. Struct. Dynam. 1 (3), 283–291.
Beltagy, I., Peters, M.E., Cohan, A., 2020. Longformer: the long-document transformer. https://doi.org/10.48550/arXiv.2004.05150.
Brown, T.B., 2020. Language models are few-shot learners. https://doi.org/10.48550/arXiv.2005.14165.
Byvatov, E., Schneider, G., 2003. Support vector machine applications in bioinformatics. Appl. Bioinf. 2 (2), 67–77.
Chen, W.F., Liu, X.L., 1990. Limit Analysis in Soil Mechanics. Elsevier Science Publishers B.V., Amsterdam, Netherlands.
Chen, X.J., Fu, Y., Liu, Y., 2022. Random finite element analysis on uplift bearing capacity and failure mechanisms of square plate anchors in spatially variable clay. Eng. Geol. 304, 106677.
Chen, X., Li, J., 2017. A subset multicanonical Monte Carlo method for simulating rare failure events. J. Comput. Phys. 344, 23–35.
Chen, X., Li, D., Tang, X., Liu, Y., 2021. A three-dimensional large-deformation random finite-element study of landslide runout considering spatially varying soil. Landslides 18 (9), 3149–3162.
Chen, X., Ren, S., Yao, K., Sousa, R.L., 2025. Large-deformation finite-element modeling of seismic landslide runout: 3D probabilistic analysis with cross-correlated random field. J. Rock Mech. Geotech. Eng. 17, 385–398.
Child, R., Gray, S., Radford, A., Sutskever, I., 2019. Generating long sequences with sparse transformers. https://doi.org/10.48550/arXiv.1904.10509.
Ching, J., Phoon, K.K., Hu, Y.G., 2009. Efficient evaluation of reliability for slopes with circular slip surfaces using importance sampling. J. Geotech. Geoenviron. Eng. 135 (6), 768–777.
Choromanski, K., Likhosherstov, V., Dohan, D., et al., 2020. Rethinking attention with performers. https://doi.org/10.48550/arXiv.2009.14794.
Chowdhury, R.N., Xu, D.W., 1995. Geotechnical system reliability of slopes. Reliab. Eng. Syst. Saf. 47 (3), 141–151.
Dang, K., Sassa, K., Fukuoka, H., et al., 2016. Mechanism of two rapid and long-runout landslides in the 16 April 2016 Kumamoto earthquake using a ring-shear apparatus and computer simulation (LS-RAPID). Landslides 13 (6), 1525–1534.
Desai, K.M., Survase, S.A., Saudagar, P.S., Lele, S.S., Singhal, R.S., 2008. Comparison of artificial neural network (ANN) and response surface methodology (RSM) in fermentation media optimization: case study of fermentative production of scleroglucan. Biochem. Eng. J. 41 (3), 266–273.
Devlin, J., 2019. BERT: Pre-Training of deep bidirectional transformers for language understanding. https://doi.org/10.48550/arXiv.1810.04805.
Fang, K., Tang, H., Li, C., Su, X., An, P., Sun, S., 2023. Centrifuge modelling of landslides and landslide hazard mitigation: a review. Geosci. Front. 14 (1), 101493.
Gariano, S.L., Guzzetti, F., 2016. Landslides in a changing climate. Earth Sci. Rev. 162, 227–252.
Goh, A.T., 1994a. Seismic liquefaction potential assessed by neural networks. J. Geotech. Eng. 120 (9), 1467–1480.
Goh, A.T., 1994b. Some civil engineering applications of neural networks. Proce. Inst. Civil Eng. – Struct. Build. 104 (4), 463–469.
Goh, A.T., 1995a. Back-propagation neural networks for modeling complex systems. Artif. Intell. Eng. 9 (3), 143–151.
Goh, A.T., 1996. Pile driving records reanalyzed using neural networks. J. Geotech. Eng. 122 (6), 492–495.
Goh, A.T.C., 1995b. Empirical design in geotechnics using neural networks. Geotechnique 45 (4), 709–714.
Graves, A., Mohamed, A., Hinton, G., 2013. Speech recognition with deep recurrent neural networks. In: 2013 IEEE International Conference on Acoustics, Speech and Signal Processing. IEEE, New York, USA, pp. 6645–6649.
Griffiths, D.V., Fenton, G.A., 2004. Probabilistic slope stability analysis by finite elements. J. Geotech. Geoenviron. Eng. 130 (5), 507–518.
Griffiths, D.V., Lane, P.A., 1999. Slope stability analysis by finite elements. Geotechnique 49 (3), 387–403.
Gu, J., Wang, Z., Kuen, J., et al., 2018. Recent advances in convolutional neural networks. Pattern Recogn. 77, 354–377.
Gurney, K., 2018. An Introduction to Neural Networks. CRC Press, London, UK.
He, X., Xu, H., Sabetamal, H., Sheng, D., 2020. Machine learning aided stochastic reliability analysis of spatially variable slopes. Comput. Geotech. 126, 103711.
He, K., Zhang, X., Ren, S., Sun, J., 2016. Deep residual learning for image recognition. In: 2016 IEEE Conference on Computer Vision and Pattern Recognition (CVPR). IEEE, New York, USA, pp. 770–778.
He, X., Xu, H., Sheng, D., 2024. Ready-to-use deep-learning surrogate models for problems with spatially variable inputs and outputs. Acta Geotech. 18 (4), 1681–1698.
Hornik, K., Stinchcombe, M., White, H., 1989. Multilayer feedforward networks are universal approximators. Neural Netw. 2 (5), 359–366.
Hsiao, C.H., Chen, A.Y., Ge, L., Yeh, F.H., 2022. Performance of artificial neural network and convolutional neural network on slope failure prediction using data from the random finite element method. Acta Geotech. 17 (12), 5801–5811.
Huang, J., Zhan, W., Xiong, C., Chen, W., 2023. Review on deep learning models for slope stability analysis. Eng. Geol. 311, 106902.
Kang, F., Xu, Q., Li, J., 2016. Slope reliability analysis using surrogate models via new support vector machines with swarm intelligence. Appl. Math. Model. 40 (11–12), 6105–6120.
Kaymaz, I., McMahon, C.A., 2005. A response surface method based on weighted regression for structural reliability analysis. Probab. Eng. Mech. 20 (1), 11–17.
Kiranyaz, S., Avci, O., Abdeljaber, O., Ince, T., Gabbouj, M., Inman, D.J., 2021. 1D convolutional neural networks and applications: a survey. Mech. Syst. Signal Process. 151, 107398.
Krabbenhoft, K., Lyamin, A.V., 2012. Computational Cam clay plasticity using second-order cone programming. Comput. Methods Appl. Mech. Eng. 209, 239–249.
Krabbenhøft, K., 2009. A variational principle of elastoplasticity and its application to the modeling of frictional materials. Int. J. Solid Struct. 46 (3–4), 464–479.
Krabbenhoft, K., Karim, M.R., Lyamin, A.V., Sloan, S., 2012. Associated computational plasticity schemes for nonassociated frictional materials. Int. J. Numer. Methods Eng. 90 (9), 1089–1117.
Krabbenhøft, K., Lyamin, A.V., Sloan, S.W., 2007. Formulation and solution of some plasticity problems as conic programs. Int. J. Solid Struct. 44 (5), 1533–1549.
Krabbenhøft, K., Lyamin, A.V., Hjiaj, M., Sloan, S.W., 2005. A new discontinuous upper bound limit analysis formulation. Int. J. Numer. Methods Eng. 63 (7), 1069–1088.
Krizhevsky, A., Sutskever, I., Hinton, G.E., 2017. Imagenet classification with deep convolutional neural networks. Commun. ACM 60 (6), 84–90.
Kroese, D.P., Brereton, T., Taimre, T., Botev, Z.I., 2014. Why the Monte Carlo method is so important today. WIREs Comput. Stat. 6 (6), 386–392.
LeCun, Y., Bengio, Y., Hinton, G., 2015. Deep learning. Nature 521 (7553), 436–444.
Li, J.P., Jiang, S.H., Ma, G.T., Rezania, M., Nezhad, M.M., Wan, J.H., 2025. Probabilistic evaluation of landslide influence zones considering stratigraphic dips and nonstationarity of soil properties. Comput. Geotech. 177, 106815.
Liu, G.R., Trung, N., 2016. Smoothed Finite Element Methods. CRC Press, London, UK.

Liu, G.R., Dai, K.Y., Nguyen, T., 2007. A smoothed finite element method for mechanics problems. Comput. Mech. 39, 859–877.
Liu, G.R., Nguyen, T.T., Dai, K.Y., Lam, K., 2006. Theoretical aspects of the smoothed finite element method (SFEM). Int. J. Numer. Methods Eng. 71 (8), 902–930.
Liu, X., Wang, Y., 2021. Probabilistic simulation of entire process of rainfall-induced landslides using random finite element and material point methods with hydro-mechanical coupling. Comput. Geotech. 132, 103989.
Liu, Y., Chen, X., Hu, M., 2023. Three-dimensional large deformation modeling of landslides in spatially variable and strain-softening soils subjected to seismic loads. Can. Geotech. J. 60 (4), 426–437.
Liu, Z., Shao, J., Xu, W., Chen, H., Zhang, Y., 2014. An extreme learning machine approach for slope stability evaluation and prediction. Nat. Hazards 73, 787–804.
Lyamin, A.V., Sloan, S.W., 2002a. Lower bound limit analysis using non-linear programming. Int. J. Numer. Methods Eng. 55 (5), 573–611.
Lyamin, A.V., Sloan, S.W., 2002b. Upper bound limit analysis using linear finite elements and non-linear programming. Int. J. Numer. Anal. Methods GeoMech. 26 (2), 181–216.
Ma, G.T., Rezania, M., Mousavi Nezhad, M., Shi, B.T., 2022b. Post-failure analysis of landslides in spatially varying soil deposits using stochastic material point method. Rock Soil Mech. 43 (7), 2003–2014 (in Chinese).
Ma, G., Rezania, M., Nezhad, M.M., 2022a. Stochastic assessment of landslide influence zone by material point method and generalized geotechnical random field theory. Int. J. GeoMech. 22 (4), 04022002.
Ma, G., Rezania, M., Nezhad, M.M., Phoon, K.K., 2024. Multivariate copula-based framework for stochastic analysis of landslide runout distance. Reliab. Eng. Syst. Saf. 250, 110270.
MOSEK ApS, 2015. The MOSEK Optimization Toolbox for MATLAB Manual. MOSEK ApS, Copenhagen, Denmark.
Mikolov, T., Karafiát, M., Burget, L., Cernocký, J., Khudanpur, S., 2010. Recurrent neural network based language model. Interspeech 2 (3), 1045–1048.
Müller, S., Schüler, L., Zech, A., Heße, F., 2022. GSTools v1. 3: a toolbox for geostatistical modelling in Python. Geosci. Model Dev. (GMD) 15 (7), 3161–3182.
Nguyen, H.C., 2020. Safety factor and failure mechanism in geotechnical engineering: a numerical study. In: Prashant, A., Sachan, A., Desai, C. (Eds.), Advances in Computer Methods and Geomechanics. Springer, Singapore, pp. 121–129.
Nguyen, H.C., 2021a. The use of adaptive smoothedfinite-element limit analysis for seismic stability of tunnels. In: Elshafie, M., Viggiani, G., Mair, R. (Eds.), Geotechnical Aspects of Underground Construction in Soft Ground. CRC Press, London, UK, pp. 330–336.
Nguyen, H.C., 2021b. Upper bound analysis of seismic stability of tunnels using cell-based smoothed finite element. In: Elshafie, M., Viggiani, G., Mair, R. (Eds.), Geotechnical Aspects of Underground Construction in Soft Ground. CRC Press, London, UK, pp. 337–342.
Nguyen, H.C., 2023. A mixed formulation of limit analysis for seismic slope stability. Géotech. Lett. 13 (1), 54–64.
Nguyen, H.C., Vo-Minh, T., 2022a. Calculation of seismic bearing capacity of shallow strip foundations using the cell-based smoothed finite element method. Acta Geotech. 17 (8), 3567–3590.
Nguyen, H.C., Vo-Minh, T., 2022b. The use of the node-based smoothed finite element method to estimate static and seismic bearing capacities of shallow strip footings. J. Rock Mech. Geotech. Eng. 14 (1), 180–196.
Nguyen, H.C., Xu, H., Nazem, M., Sousa, R., Kowalski, J., Zhao, Q., 2025b. Deep-learning surrogate models for the stability of a wide rectangular tunnel. Comput. Geotech. 179, 106946.
Nguyen, H.C., Zhang, X., Nazem, M., 2025a. A mixed smoothed finite element limit analysis formulation for static and seismic collapse loads. Acta Geotech. 20, 323–345.
Nguyen, H.C., Nguyen-Son, L., 2022. A stable CS-FEM for the static and seismic stability of a single square tunnel in the soil where the shear strength increases linearly with depth. J. Rock Mech. Geotech. Eng. 14 (4), 1253–1265.
Onate, E., Idelsohn, S.R., Celigueta, M.A., Rossi, R., Marti, J., Carbonell, J.M., Suárez, B., 2011. Advances in the particle finite element method (PFEM) for solving coupled problems in engineering. In: Oñate, E., Owen, R. (Eds.), Particle-Based Methods: Fundamentals and Applications. Springer, Dordrecht, Dordrecht, pp. 1–49.
Phoon, K.K., Kulhawy, F.H., 1999. Characterization of geotechnical variability. Can. Geotech. J. 36 (4), 612–624.
Phoon, K.K., Zhang, W., 2023. Future of machine learning in geotechnics. Georisk 17, 7–22.
Ren, S.P., Chen, X.J., Ren, Z.L., Cheng, P., Liu, Y., 2023. Large-deformation modelling of earthquake-triggered landslides considering non-uniform soils with a stratigraphic dip. Comput. Geotech. 159, 105492.
Sakellariou, M.G., Ferentinou, M.D., 2005. A study of slope stability prediction using neural networks. Geotech. Geol. Eng. 23, 419–445.
Szegedy, C., Liu, W., Jia, Y., et al., 2015. Going deeper with convolutions. In: 2015 IEEE Conference on Computer Vision and Pattern Recognition (CVPR). IEEE, New York, USA, pp. 1–9.
Taigman, Y., Yang, M., Ranzato, M., Wolf, L., 2014. Deepface: closing the gap to human-level performance in face verification. In: 2014 IEEE Conference on Computer Vision and Pattern Recognition. IEEE, New York, USA, pp. 1701–1708.
Tang, H.M., Liu, X., Hu, X.L., Griffiths, D.V., 2015. Evaluation of landslide mechanisms characterized by high-speed mass ejection and long-run-out based on events following the Wenchuan earthquake. Eng. Geol. 194, 12–24.
Turner, A.K., 2018. Social and environmental impacts of landslides. Innov. Infrastruct. Solut. 3 (1), 70.
Valagussa, A., Marc, O., Frattini, P., Crosta, G.B., 2019. Seismic and geological controls on earthquake-induced landslide size. Earth Planet Sci. Lett. 506, 268–281.
Vaswani, A., Shazeer, N., Parmar, N., et al., 2017. Attention is all you need. In: Proceedings of the 31st International Conference on Neural Information Processing Systems (NIPS'17). Curran Associates Inc., Red Hook, USS, pp. 6000–6010.
Vo-Minh, T., Nguyen, H.C., 2022. Seismic stability of a circular tunnel in cohesive-frictional soils using a stable node-based smoothed finite element method. Tunn. Undergr. Space Technol. 130, 104606.
Wang, L., Zhang, X., Zaniboni, F., Oñate, E., Tinti, S., 2021a. Mathematical optimisation problems for particle finite element analysis applied to 2D landslide modeling. Math. Geosci. 53 (1), 81–103.
Wang, H., Moayedi, H., Kok Foong, L., 2021b. Genetic algorithm hybridized with multilayer perceptron to have an economical slope stability design. Eng. Comput. 37, 3067–3078.
Wang, S., Li, B.Z., Khabsa, M., Fang, H., Ma, H., 2020. Linformer: Self-Attention with linear complexity. https://doi.org/10.48550/arXiv.2006.04768.
Wang, Z.Z., 2022. Deep learning for geotechnical reliability analysis with multiple uncertainties. J. Geotech. Geoenviron. Eng. 148 (4), 06022001.
Wang, Z.Z., Goh, S.H., 2021. Novel approach to efficient slope reliability analysis in spatially variable soils. Eng. Geol. 281, 105989.
Xing, A., Wang, G., Li, B., Jiang, Y., Feng, Z., Kamai, T., 2014. Long-runout mechanism and landsliding behaviour of large catastrophic landslide triggered by heavy rainfall in Guanling, Guizhou, China. Can. Geotech. J. 52 (7), 971–981.
Xu, H., He, X., Sheng, D., 2022. Rainfall-induced landslides from initialization to post-failure flows: stochastic analysis with machine learning. Mathematics 10 (23), 4426.
Xu, H., He, X., Pradhan, B., Sheng, D., 2023. A pre-trained deep-learning surrogate model for slope stability analysis with spatial variability. Soils Found. 63 (3), 101321.
Zhang, H., Nguyen, H., Bui, X.N., Pradhan, B., Asteris, P.G., Costache, R., Aryal, J., 2022. A generalized artificial intelligence model for estimating the friction angle of clays in evaluating slope stability using a deep neural network and Harris Hawks optimization algorithm. Eng. Comput. 38, 3901–3914.
Zhang, L., Zhang, Y., 2021. Machine learning algorithms for slope stability prediction: a comprehensive review. Comput. Geotech. 137, 104237.
Zhang, X., Krabbenhoft, K., Sheng, D., 2014. Particle finite element analysis of the granular column collapse problem. Granul. Matter 16, 609–619.
Zhang, X., Krabbenhoft, K., Pedroso, D.M., Lyamin, A.V., Sheng, D., Da Silva, M.V., Wang, D., 2013. Particle finite element analysis of large deformation and granular flow problems. Comput. Geotech. 54, 133–142.
Zhang, Y., Zhang, X., Li, X., 2024b. Numerical investigation of punch-through mitigation in stiff-over-soft clays using skirted spudcan. Ocean. Eng. 312, 119170.
Zhang, Y., Zhang, X., Li, X., Lingden, A., Meng, J., 2024a. Numerical analysis of downward progressive landslides in long natural slopes with sensitive clay. J. Rock Mech. Geotech. Eng. 16, 3937–3950.
Zhang, Y., Zhang, X., Nguyen, H., Li, X., Wang, L., 2023. An implicit 3D nodal integration-based PFEM (N-PFEM) of natural temporal stability for dynamic analysis of granular flow and landslide problems. Comput. Geotech. 159, 105434.

Dr. Haoding Xu is currently a Lecturer at Xi'an University of Technology (XUT), China, where he also served as the Deputy Director of the XUT Institute of Geotechnical Engineering. In this role, he worked closely alongside Profs. Faning Dang, Caihui Zhu, and Qin Zhao, whose significant mentorship and collaboration have been instrumental in advancing his research career. Dr. Xu's primary research focus is on the development of numerical computation methods and machine learning techniques, with substantial experience in the creation of surrogate models. Prior to his current position, Dr. Xu held a Postdoctoral Research Associate position from February to October 2023 at the University of Technology Sydney (UTS) within the research team led by Distinguished Prof. Daichao Sheng. During this time, he concentrated on integrating surrogate models with numerical methods to investigate geotechnical engineering stability analysis and large deformation problems. Dr. Xu finished his PhD in Geotechnical Engineering from UTS, under the supervision of Distinguished Professor Daichao Sheng and Senior Lecturer Xuzhen He. His doctoral studies at UTS were supported by the Faculty of Engineering and Information Technology Scholarship and the International Research Scholarship.